UiT The Arctic University of Norway

Faculty of Science and Technology
Department of Physics

Design and implementation of an oblique ionosonde receiver

For studies of spatial and temporal ionospheric structures

Jens Floberg

FYS-3931 Master thesis in Space Physics 30 SP
1 June 2022

This thesis document was typeset using the *UiT Thesis LaTeX Template*.

To my late great grandfather Arne Reiulf, the eternal technologist

Abstract

The study of the ionosphere has been of central interest since its discovery in the early 20th century. In later decades there has been an increasing appreciation and need for understanding the spatial and temporal structure of the ionosphere and how the structure is affected by various processes in the atmosphere. An important process in this context is that of atmospheric gravity waves (AGWs). AGWs in the lower region of the atmosphere instigate propagating fluctuations of the electron density in the ionosphere, the signatures of which are called travelling ionospheric disturbances (TIDs). A series of methods that can be used for investigating TIDs are already in existence, but between complex techniques and expensive hardware there is still a need for access to simple and inexpensive methods of inquiry. Oblique ionosonde receivers that work with existing transmission infrastructure are a simple and inexpensive way to address this need. In this project we developed an oblique ionosonde receiver using commercially available and/or easily manufactured components. The receiver is based on software defined radio technology and utilizes a magnetic loop antenna as the driven element operating with frequencies 1-30 MHz. The receiver system is designed to be a sub-system in a network of oblique ionosonde receivers that are synchronized using GPS. Four receiver systems were built according to the design and deployed in a geographically distributed network around an existing transmitter at Sodankylä Geophysical Observatory. The fluctuation period of TIDs is governed by the buoyancy period defined by the Brunt-Väisälä frequency. The buoyancy period varies with altitude but is rarely below 5 minutes. The radar receivers built in this project are capable of operating with a better temporal resolution than 1 minute, but the resolution is limited by the transmitter antenna in Sodankylä as it performs a sweep once every minute. A temporal resolution of 1 minute allows for Nyquist sampling the Brunt-Väisälä frequency, meaning that operating the receivers in a network makes for a suitable tool to resolve the signatures of TIDs. Both the receiver design and the software used for operating the receiver are made available to the public.

Acknowledgements

First I would like to extend my gratitude to my supervisors Dr. Juha Vierinen and Dr. Devin Ray Huyghebaert. Thank you Juha for sharing with me your abundant knowledge and experience in both radar and computer science, and thank you for orchestrating such an interesting and educational thesis project. Thank you Devin for taking on the supervisor role so diligently, you were never hesitant in providing helpful discussions and instructive sessions in the laboratory. Thanks to you, the 6-day installation trip to Finland was a delightful experience. I would also like to thank Tomi Teppo, Dr. Lassi Roininen and the rest of the staff associated with Sodankylä Geophysical Observatory for helping us organize and carry out the installations in Finland. The deployment part of this thesis project would not have been possible without their aid. Many thanks to my siblings, parents and grandparents for supporting me during the last 5 years of academic pursuit. Lastly I want to thank my partner Camilla for believing in me and my project all this time.

Contents

List of Figures

List of Tables

1

Introduction

The Earth's atmosphere is bombarded with solar radiation on a constant basis. As a result, the various neutral particles present in the atmosphere are ionized, transforming upper portions of the atmosphere into a weakly ionized plasma made up of neutral particles, ions, and electrons. This layer is called the ionosphere. It's lower and upper boundaries are fluctuating with solar activity, but it is commonly reported to stretch from an altitude of about 50 km up to an altitude of about 500-600 km [Blaunstein, 2008].

An electromagnetic wave moving through the ionosphere undergoes variable degrees of absorption and refraction depending on its frequency and the ionospheric parameters. If the conditions permit it, an electromagnetic wave transmitted from the Earth's surface can be reflected back to the Earth by the ionosphere. This enables electromagnetic waves to propagate beyond the horizon, called over-the-horizon (OTH) transmission.

OTH broadcasts are particularly valuable in radio communications because they allow communication beyond the line of sight. Today, OTH broadcasts are utilized in both civilian and military applications (e.g., communication, early warning systems, and navigation), but there are also additional uses. The reflection of radiowaves is dependent on the ionosphere's properties, as mentioned briefly in the preceding paragraph. Because the qualities of the reflected signal vary as circumstances in the ionosphere change, knowledge of the transmission parameters combined with study of the reflected signal allows for exploration of ionospheric dynamics. Having the capacity to monitor ionospheric properties not only helps with anticipating radio-communications conditions, but it may also help with understanding how various events influence the ionosphere directly or indirectly. This motivates the development of a radio receiver system capable of receiving and interpreting these signals.

The goal of this project is to create a relatively low-cost, easy-to-assemble radar receiver system using open-source software and a design that is freely available to anybody who is interested. The radar receiver will function as the receiver end of an ionosonde. It is also the intention for multiple radar receiver systems to serve as subsystems in a network of receivers that are geographically distributed around a transmitter in operation. The receivers are therefore the first handful of receivers to be part of the Network Of Ionosonde Receivers Experiment (NOIRE), an experiment spearheaded by Juha Vierinen. The radar receivers in the network are synchronized in time using GPS. Having such a synchronized network allows for investigating ionospheric dynamics over a large area, as changes in the ionospheric parameters revealed by the signal received at one location may be correlated to changes seen in the parameters revealed by the signal received at a different location. In this sense, the instrument this thesis project seeks to produce could be used to investigate spatial and temporal structures in the ionosphere. Both the instrument and this text builds on a prototype I built during a project paper in the fall of 2021. Certain segments of text have been reused from the the project paper, which is titled *Functional prototype for an oblique over-the-horizon radar receiver*.

2

Background

This chapter will cover some of the theory behind radiowave propagation in the ionosphere, and the mechanism by which the radiowaves are reflected. The chapter will also describe the concept of an ionosonde and the data collected by an ionosonde in the form of ionograms.

2.1 Ionospheric radiowave propagation

A radiowave incident on the ionospheric plasma will reflect off the plasma if the frequency of the radiowave ω is less than or equals the plasma frequency ω_p [Davies, 1965]. The plasma frequency is a characteristic property of a plasma, and is expressed as

$$\omega_p = \sqrt{\frac{n_e q^2}{m_e \epsilon_0}} \tag{2.1}$$

where n_e is the electron density, q is the elementary charge, m_e is the mass of an electron and ϵ_0 is the vacuum permittivity.

As mentioned in the introduction, the ionospheric plasma is generated mainly by solar radiation. While other phenomena such as cosmic rays or collisions also contribute to the ionization, the Sun is responsible for the majority of it. The process of oppositely charged particles recombining into neutral particles occurs simultaneously. This competes with the ionization and is mainly a collisional phenomenon [Kelley, 2009]. The amount of ionization throughout the ionosphere and the rate at which ionization occurs varies with altitude, as it depends on a series of parameters that also depend on the altitude. These parameters include (but are not limited to) the solar radiation intensity, neutral particle density and recombination rate. The intensity of the incident solar radiation decreases at lower altitudes of the ionosphere as the energy is being spent on the creation of ions. The neutral density profile arises from the hydrostatic equilibrium between two opposing influences - gravity pulling towards the Earth and the atmospheric gas pressure leading the atmospheric gases to expand outwards towards space. Figure 2.1 shows a simplified view of the altitude dependence of the solar radiation intensity, ionization rate and the neutral density. Note how the ionization rate reaches a maximum at the intersection between the radiation intensity and the neutral density. The quantities in figure 2.1 are in arbitrary scales and are included for illustrative purposes.

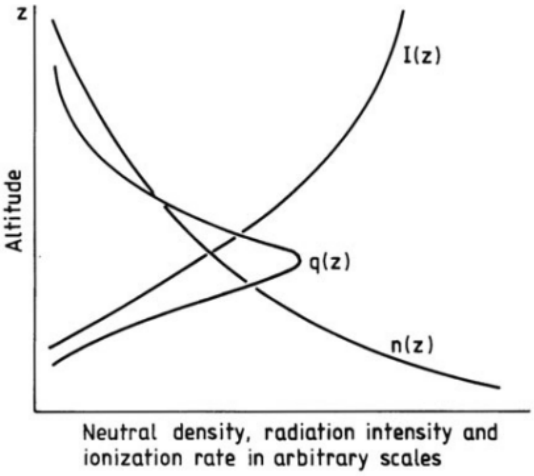

Figure 2.1: Solar radiation intensity $I(z)$, ionization rate $q(z)$ and neutral density $n(z)$ as they vary with altitude. Figure appropriated from [Brekke, 2013].

The electron density will have some proportionality with the ionization rate. This leads to the possibility of modeling the ionosphere as a series of layers with differing electron densities, first modelled by Sydney Chapman in 1931. The model is based on a few simplifying assumptions; 1) atmosphere consists of a single gas species, 2) the stratification is horizontal, 3) radiation from the Sun is parallel and monochromatic and 4) the atmosphere is isothermal, meaning the scale height is constant. A full treatment of the model is beyond the scope of this thesis, see [Chapman, 1931] for more details.

Eq. (2.1) reveals that the plasma frequency depends on the electron density, and as such ω_p varies from layer to layer as well. Radiowaves entering and exiting these layers as they travel in ionosphere will be refracted to some degree, like the refraction of light as it traverses the interface between two different media. Refraction of an electromagnetic wave travelling between two media with refractive indices n_1 and n_2 is described by Snell's law:

$$n_1 sin\theta_1 = n_2 sin\theta_2 \tag{2.2}$$

where θ_1 is the incident angle on the interface and θ_2 is the angle of refraction [Shankar, 2016]. As will be seen in the next section, the index of refraction of a plasma is related to the plasma frequency. The wave will refract away from the vertical as it traverses the ionospheric layers, until it reaches a layer in which the wave angle of incidence will result in an angle of refraction pointing back towards the ground. This is the mechanism that is utilized for OTH transmission [Davies, 1965]. Figure 2.2 illustrates the concept in a simplified manner.

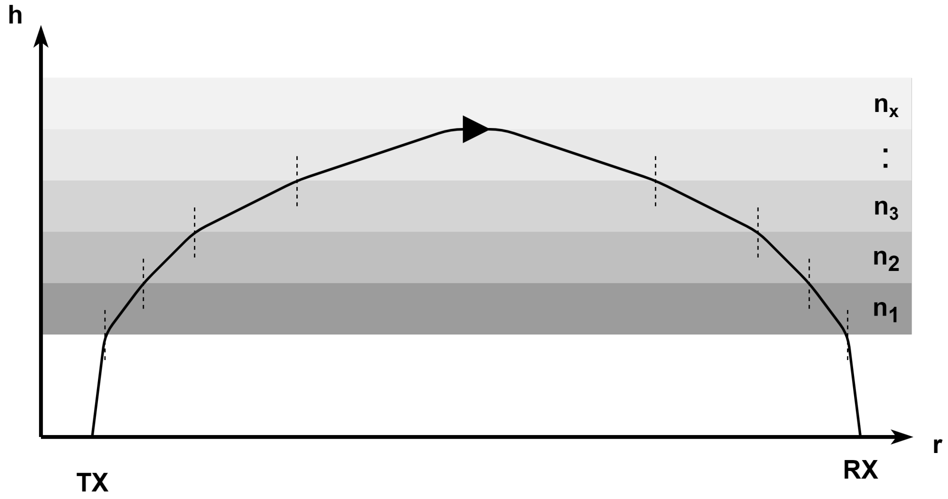

Figure 2.2: An illustration of ionospheric reflection through gradual refraction of the incident electromagnetic wave, utilized in OTH transmission. The ground harboring the transmitter (TX) and the receiver (RX) is flat in the illustration for simplicity.

2.1.1 Appleton equation

The extent of the refraction that occurs between layers depends on the refractive index n of the layer. The refractive indices of the ionospheric layers are described by the rather complicated Appleton equation, which in its full form includes the effects of the background magnetic field of the Earth and the electron-neutral collisions leading to wave absorption. It is given as [Davies, 1965];

$$n^2 = 1 - \frac{X}{1 - iZ - \left(\frac{Y_T^2}{2-2X-2iZ}\right) \pm \left(\frac{Y_T^4}{4(1-X-iZ)^2}\right)^{\frac{1}{2}} + Y_L^2} \tag{2.3}$$

with definitions

$$\begin{aligned} X &= \frac{\omega_p^2}{\omega^2} \\ Y_T &= Y sin\theta \\ Y_L &= Y cos\theta \\ Y &= \frac{\omega_g}{\omega} \\ Z &= \frac{\nu_e}{\omega} \end{aligned}$$

where θ is the angle between the incident radiowave and the magnetic field line, ω_g is the electron gyrofrequency (the angular frequency of circular electron oscillatory motion induced by the magnetic field) and ν_e is the electron-neutral collision frequency. Y_T and Y_L refers to the transverse and longitudinal components of the wave respectively (in relation to the magnetic field). This formula is rather complicated, and a full treatment of it is beyond the scope of this thesis. A simplified case will be addressed however, one in which we assume no magnetic field and no electron-neutral collisions. These phenomena are present in the real ionosphere, and must be accounted for in any application of the equation where accuracy is of importance. With $B = 0 \implies \omega_g \approx 0$, in addition to $\nu_e \approx 0$, the Appleton equation simplifies to

$$n^2 = 1 - X = 1 - \frac{\omega_p^2}{\omega^2} \tag{2.4}$$

Looking at radiowave propagation starting in the lower layers of the ionosphere, we have $\omega > \omega_p$ (the wave travels upwards and is not reflected off the current layer). If we now consider the fact that ω_p is proportional to the electron density n_e, and that n_e varies with ionization rate in the fashion exhibited in figure 2.1, we realize that at some point during the wave propagation the plasma frequency ω_p will equal the wave frequency ω (assuming that ω is less than the peak plasma frequency). At this point, the fraction $\frac{\omega_p^2}{\omega^2}$ evaluates to unity leading eq. (2.3) to go to zero. In line with Snell's law of refraction, this means that the wave achieves total internal reflection and is directed back towards the Earth. The highest frequency at which this occurs is often called the *critical frequency*. The critical frequency f_c is related to the electron density n_e by looking at the frequency corresponding to the peak plasma frequency ω_p:

$$\omega_p = \sqrt{\frac{n_e q^2}{m_e \epsilon_0}} \Rightarrow f_c = \frac{1}{2\pi}\sqrt{\frac{n_e q^2}{m_e \epsilon_0}} \Rightarrow f_c \approx 9\sqrt{n_e} \tag{2.5}$$

where q is the elementary charge, m_e is the electron mass and ϵ_0 is the permittivity of free space. Keeping in mind that the ionization rate as seen in figure 2.1 reaches a maximum at some altitude before it decreases again with further increase in altitude, we also know that the electron density will reach some maximum as well. This means that there is a limit to the wave frequency that can be reflected off the ionosphere. This frequency is often called the *maximum usable frequency*, or MUF. Frequencies above the MUF simply penetrates the ionosphere and escape into space, regardless of the angle of incidence.

2.1.2 Modes of radiowave propagation in a magnetized plasma

The ionosphere is considered a weakly ionized plasma, magnetized by the magnetic field of the Earth. Due to the magnetic field of the Earth, the ionosphere is a birefringent medium, meaning that the refractive index of the medium depends on the polarization of the incident wave. Electromagnetic waves travelling in magnetized plasma will be decomposed into two modes of propagation, depending on their polarization [Davies, 1965]. These two modes are known as the ordinary mode (O-mode) and the extraordinary mode (X-mode). The next paragraph takes a closer look into the O- and X-modes, based on discussion and derivations made by Chen [Chen, 1983].

Consider a radiowave propagating perpendicular to the magnetic field $\boldsymbol{B}_0 = B_0\hat{z}$, so that $\boldsymbol{k} \perp \boldsymbol{B}_0$. For a plane polarization, the electric field component $\boldsymbol{E}_1 = E_1\hat{z}$ of the radiowave is parallel to the magnetic field, $\boldsymbol{E}_1 \parallel \boldsymbol{B}_0$. As the electron motion induced by the electric field is parallel to $\boldsymbol{B}_0$, it is unaffected by $\boldsymbol{B}_0$. This wave propagates in the same manner as an equivalent wave in an unmagnetized plasma where $\boldsymbol{B}_0 = 0$, and is called the O-mode. The dispersion relation for the ordinary wave is

$$\omega^2 = \omega_p^2 + c^2k^2 \;\Rightarrow\; \frac{c^2k^2}{\omega^2} = 1 - \frac{\omega_p^2}{\omega^2} \tag{2.6}$$

which is the same as the dispersion relation for the electromagnetic wave travelling in an unmagnetized plasma.

Let us instead consider the case where $\boldsymbol{k} \perp \boldsymbol{B}_0$, but the electric field component is perpendicular to the magnetic field, $\boldsymbol{E}_1 \perp \boldsymbol{B}_0$. According to [Chen, 1983], most waves with this property are elliptically polarized rather than plane polarized, meaning that they will have electric field components in both the $\hat{\boldsymbol{x}}$- and $\hat{\boldsymbol{y}}$-directions:

$$\boldsymbol{E}_1 = E_x\hat{\boldsymbol{x}} + E_y\hat{\boldsymbol{y}}$$

In this case, the electron motion induced by the electric field will be affected by $\boldsymbol{B}_0$. Including this in the derivation leads to a more complex expression for the corresponding dispersion relation:

$$\frac{c^2k^2}{\omega^2} = 1 - \frac{\omega_p^2}{\omega^2}\frac{\omega^2 - \omega_p^2}{\omega^2 - \omega_h^2} \tag{2.7}$$

where $\omega_h^2 = \omega_p^2 + \omega_c^2$ is the upper hybrid frequency and $\omega_c = \frac{|q|B}{m}$ is the cyclotron frequency. This dispersion relation shows that the strength of the magnetic field affects how the extraordinary wave is reflected, and the fact that more than one mode for propagation exists means that there are more than one possible path the radiowave can travel. The derivations of these dispersion relations can be found in [Chen, 1983].

Measurements made by an ionosonde in the form of an ionogram will show traces of two ionospheric echoes for a single radiowave transmission, because of the two possible modes of propagation. The echoes are similar in shape but slightly offset in frequency. In later chapters of this thesis we will provide some measurements exhibiting the traces for both modes.

2.2 Ionosondes

Ionospheric reflection is the phenomenon exploited by *ionosondes*, which are radar instruments used to investigate the ionosphere. While a wide range of different ionosonde systems have been previously implemented, some examples include the Digisonde-128PS [Reinisch, 1978] and the Dynasonde 21 [Zabotin, 2005]. As a basic description, an ionosonde consists of a radio transmitter and a radio receiver with analogue and/or digital analysis tools. The transmitter will transmit radiowaves that travel into the ionosphere until they are reflected, as described in the previous section, with the receiver continually listening for the reflected signal. The transmitted signal is swept across a range of frequencies in the high-frequency spectrum. This is usually done starting from a small frequency and increasing, leading to this type of signals to be named "chirps". In figure 2.3, a block diagram displaying the basic components of a chirp ionosonde is shown.

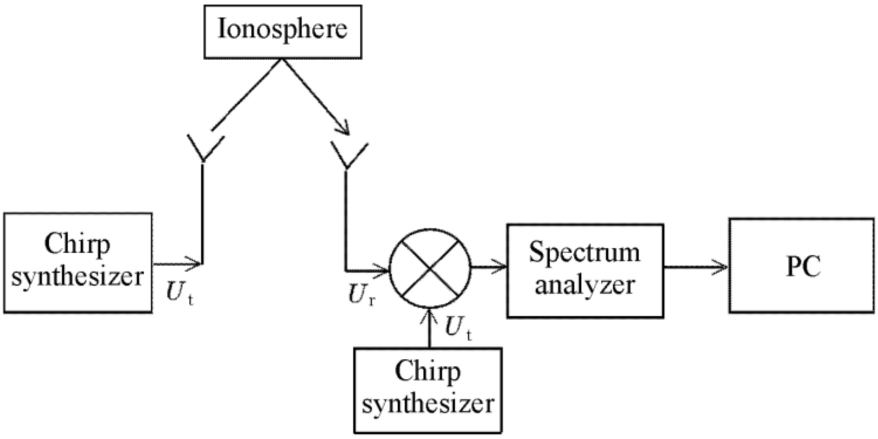

Figure 2.3: Block diagram of a chirp ionosonde. Diagram adapted from [Ivanov, 2003].

As the plasma frequency varies with altitude across the different layers, waves of different frequencies will reflect off different layers. Using the wave travel time (that can be related to a height in the ionosphere), the receiver records and maps which frequencies are reflected at which times/heights. This information is graphically presented in an *ionogram*.

Radiowaves can be transmitted at vertical incidence, which is a monostatic situation where the transmitter and receiver are in the same location. The radiowave is transmitted directly overhead, and the receiver makes measurements of the signal that reflects directly back to it. Vertical sounding gives insight into the ionosphere region directly overhead, making it more suitable for diagnostic inquiry into the radio transmission conditions in the vicinity of a facility [Ivanov, 2003]. Alternatively, the radiowave can be transmitted at an oblique angle relative to the vertical. This is a bistatic situation, as the transmitter and the receiver are located in different locations. The main difference is in how far the wave will travel, depending on the angle of incidence. Oblique transmission results in a longer range for the signal. It also has an advantage over vertical incidence when it comes to coverage. A single vertical incidence ionosonde will only be able to measure what is going on in the region of the ionosphere directly overhead, while oblique incidence ionosondes enable a single transmitter to communicate with several receivers covering a larger ionospheric region of interest. Oblique sounding is useful for studying the ionospheric conditions along the radiowave travelpath [Ivanov, 2003]. The radio receiver system designed and built in this project can serve as the receiver in an oblique sounder.

2.3 Ionograms

The information obtained by an ionosonde is typically presented graphically in the form of an ionogram. An ionogram typically plots the wave travel time (y-axis) as a function of frequency (x-axis). Also common is to use the *virtual height* on the y-axis, which is related to the travel time via

$$h' = \frac{ct}{2}$$

and is the altitude that the radiowave received must have been reflected from given the measured travel time (this assumes no delays of the signal, such as multi-path travel). Here c is the speed of light and t is the elapsed time [Davies, 1965]. An important note is that the virtual height h' is not the actual height of reflection, but rather the height corresponding to perfect, mirror-like reflection. In reality and in line with the Appleton equation, the radiowave will refract between the layers with differing refractive indices and therefore spend some amount of time travelling horizontally. This leads to a discrepancy between the virtual height and the actual height. There are relationships between the virtual height and the actual height that makes the virtual height useful. The different paths are further described and illustrated in section 2.3.1. The travel time is relative to the time of initial signal transmission and signal reception, necessitating synchronization between the transmitter and the receiver. In this ionosonde receiver project, GPS timing is used for synchronization. Other electronic means and even mechanical means have been used for synchronization in the past.

Depending on whether you have vertical or oblique incidence, the ionospheric trace that can be seen in an ionogram will have a slightly different appearance. For vertical incidence, the radiowave simply travels in a more or less straight line directly overhead until it encounters a layer in the ionosphere where the electron density gradient is steep enough for it to hit the critical frequency and become reflected. The resulting ionospheric trace that can be seen in the corresponding ionogram has the shape indicated in figure 2.4a), which indicates that the virtual height increases with the frequency in a parabolic fashion until it reaches the frequency reaches critical frequency, meaning any larger frequencies than this will not be reflected and will escape into space.

For oblique incidence, the radiowave is incident on the ionosphere with an angle relative to the normal. This allows the wave to have a longer travel path in the ionosphere than for vertical incidence with a wave of equal frequency, but it will only penetrate to a lower altitude before being reflected. If a wave of frequency f_{ob} hits the ionosphere obliquely at angle α it will reflect in the same manner (including not reflecting at all) as vertical incident wave of frequency $f_v = \frac{f_{ob}}{cos\alpha}$ [Davies, 1965]. The oblique ionogram appears with more of a nose-like structure, as can be seen in figure 2.4.

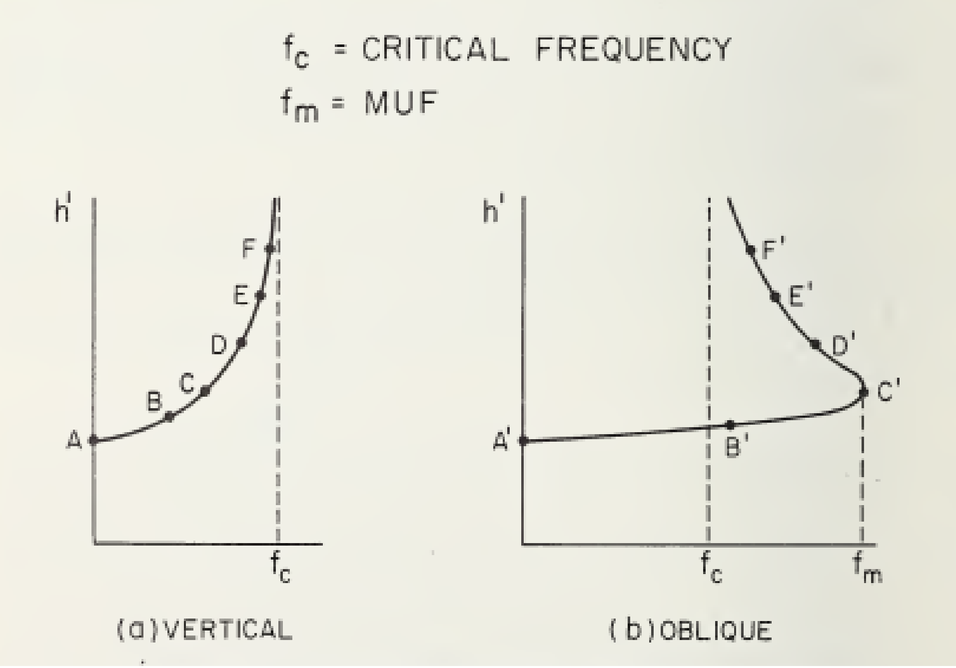

Figure 2.4: Comparison between a) vertical incidence ionogram and b) oblique incidence ionogram. Figure adapted from [Davies, 1965].

2.3.1 Equivalence relationships

Ionograms, despite using a virtual height, retain their usefulness because of the relationships that exist between the virtual height and the actual height. This subsection will have a short look at the most important ones when assuming a plane ionosphere, but a full treatment of these are outside the scope of the thesis. Further complications arise when a spherical model of the ionosphere is adopted, Davies provides more details on the matter [Davies, 1965].

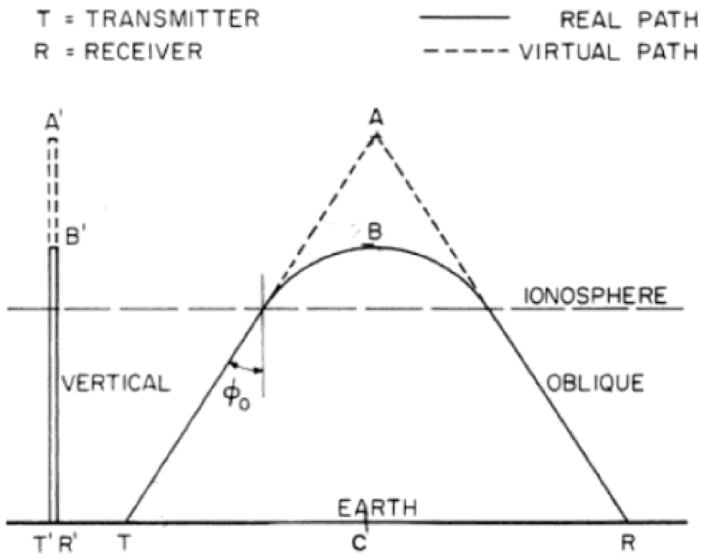

Figure 2.5: Diagram showing both oblique and vertical sounding, where the solid lines are the actual path and the dotted lines the equivalent triangular paths. Diagram is adapted from [Davies, 1965].

Breit and Tuve theorem

The scientists Breit and Tuve are credited with constructing the first ionosonde, and with proving the existence of the ionosphere in 1926 [Breit, 1926]. In doing so they also formulated an equivalence theorem. With figure 2.5 in mind, Davies writes that the theorem states that the equivalent path P' for transmissions between a transmitter T and a receiver R is given by the length of the equivalent triangle TAR [Davies, 1965];

$$P' = TA + AR \tag{2.8}$$

This assumes that both the transmitter and the receiver are located outside the ionosphere. This can be formulated in another way, somewhat closer to what Breit and Tuve themselves wrote [Breit, 1926]. Consider a wave travelling in the ionosphere, retarded by interaction with the medium. The theorem states that the travel time for this wave travelling along the actual path TBR is the same as the travel time of a non-slowed wave travelling along the virtual path TAR. Non-slowed wave in this context refers to if the wave is travelling in free space. This equivalence of the travel times relates the virtual path to the actual path.

Martyn's theorem

Martyn's theorem states that if f_{ob} and f_v are equivalent frequencies of waves reflected obliquely and vertically from the same real height, then the virtual height of reflection of f_v is equal to the virtual height of reflection of f_{ob}. In other words, the virtual height of reflection of f_v is equal to the height of the equivalent triangular path for the oblique signal [Davies, 1965]. With respect to the diagram in figure 2.5, Martyn's theorem states that

$$B' = B \implies A' = A \tag{2.9}$$

2.3.2 Scaling

The process of scaling an ionogram is the process of extracting usable parameters from an ionogram image. These parameters include the critical frequencies (for different wave propagation modes) and virtual heights for the different layers in the ionosphere. The layers differ from each other with the respect to electron density and subsequently also plasma frequency. Although the altitude boundaries of the regions varies in reports, the three main regions of the ionosphere are [Piggott, 1978]:

- **D-region:** The D-region is the ionized region stretching from 75 km to 95 km above the surface of the Earth. Sustained by the radiation from the Sun, the D-region disappears during night-time. Waves with frequencies that are typically reflected from higher layers experience absorption in the E-region.

- **E-region:** The E-region is the ionized region stretching from 95 km to about 150 km altitude. The ionization in the region is weakened but does not disappear during night-time. The region is also host to a phenomenon called sporadic-E, or E$_s$, which is an event in which a layer at E-region altitude sporadically appears with intense increase in ionization, leading to the possibility of reflecting radiowaves of much higher frequency than usually possible for E-region altitudes [Kirkwood, 2000].

- **F-region:** The F-region is the ionized region above 150 km altitude. The F-region is central for reflecting radiowaves as it exists throughout both day and night. During day-time it is typically divided into the F1- and the F2-layer, with the F2-layer being the most widely used in high-frequency radiowave communication. During night-time, the layers in the F region merge into a single F2 layer.

Scaling an ionogram will yield measurements of the critical frequencies and minimum virtual heights of the different layers. While there are a long list of parameters that are possible to extract from an ionogram using various techniques, the most important parameters for this thesis are listed below. This is based on ionogram scaling manuals that are well known in the field [Piggott, 1978], [Wakai, 1987]:

- **foF2** - the ordinary wave critical frequency of the F2 layer (the uppermost layer in the F-region). Extracted from the ionogram by looking at the frequency that the trace of the ordinary wave approaches when the wave fully penetrates the ionosphere and escapes

- **h'F** - the minimum virtual height of the ordinary wave trace in the F-region. The minimum virtual height is measured where the trace is horizontal.

- **foE** - the ordinary wave critical frequency corresponding to the lowest thick layer in the E region. The frequency is measured at the point where the ordinary trace appears to have a discontinuity, as indicated in figure 2.6.

- **h'E** - the minimum virtual height of the normal E layer taken as a whole. The minimum virtual height is measured where the trace is horizontal.

There are other parameters as well, summarized in figure 2.6. The other parameters include critical frequencies and virtual heights for the traces corresponding to the extraordinary wave. The layers separated within a region also have their own parameters, such as **h'F1** and **foF1**. There are also parameters used to describe the virtual heights and critical frequencies characterizing specific phenomenon. A central example is sporadic-E, with parameters **foEs** and **h'Es**.

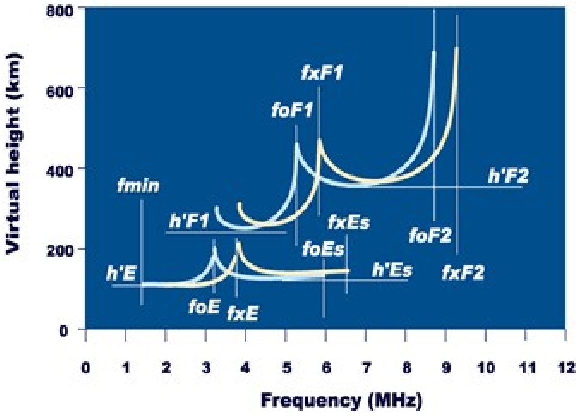

Figure 2.6: An illustration showing where the ionospheric parameters can be found in an ionogram. Image downloaded from `http://iono-gnss.kmitl.ac.th/?page_id=355`.

Manually scaling ionograms is a tedious job requiring a qualified worker if the parameters are to be scaled with any accuracy. The traditional manuals include a range of classification strategies and methods for accurate scaling [Piggott, 1978],[Wakai, 1987]. There are however efforts being made to implement automatic ionogram scaling software reinforced by machine learning algorithms [Xiao, 2020].

2.4 Applications of an oblique ionosonde receiver

The oblique ionosonde receiver this project aims to implement can be used to study spatial and temporal variations in the ionosphere. A considerable share of these variations are ionospheric manifestations of atmospheric gravity waves (AGWs), known as travelling ionospheric disturbances (TIDs) [Hocke, 1996]. TIDs are ionospheric structures that propagate in the ionosphere, contributing to the high degree of electron density variability. The sources for AGWs can be man-made or natural mechanisms, including nuclear explosions, thunderstorms, neutral winds affected by topography, geomagnetic storms and auroral events [Hunsucker, 1982].

TIDs are classified by their scale size. Large-scale TIDs (LSTID) typically have horizontal velocities of 300-1000 m/s, 100-3000 km wavelengths and periods from 1 hour to more than 2 hours. Medium-scale TIDs (MSTID) have horizontal velocities of 100-300 m/s, 200-500 km wavelength and periods of 15 minutes to 1 hour [Jonah, 2018]. The TID period of oscillation is important as it affects the sampling frequency that must be employed in order to temporally resolve the structures. Generally in a stable atmosphere, displacing an air parcel from its equilibrium position leads to an oscillation around said equilibrium. This is described by the Brunt-Väisälä frequency [Kelley, 2009]. The corresponding period is called the buoyancy period, and figure 2.7 displays how it varies with altitude.

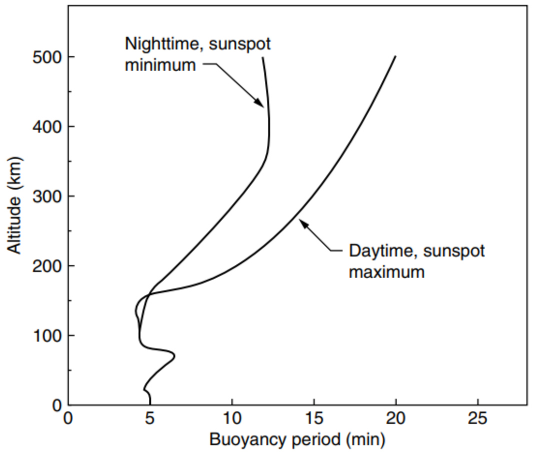

Figure 2.7: Buoyancy period as it varies with altitude. Figure adapted from [Kelley, 2009].

If AGWs are to be resolved temporally, the ionosphere must be Nyquist sampled. This means using a sampling frequency of at least twice the Brunt-Väisälä frequency, or equivalently the sampling period must be half that of the buoyancy period. With appropriate sampling frequency, it is possible to see the signatures of TIDs in time series produced from measurements made by ionosondes. Reinisch et al provides measurements of electron isodensity contours derived from Digisonde vertical ionogram measurements [Reinisch, 2018]. Quasi-periodic height variations can be seen in figure 2.8, which is the signature of a TID passing by the site of vertical sounding.

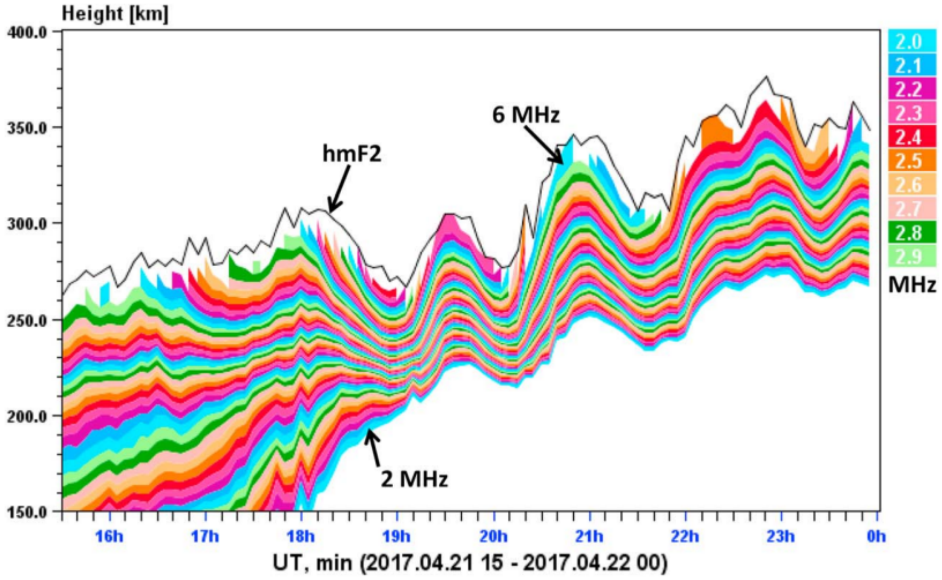

Figure 2.8: TID signatures seen as height variations in the electron isodensity contours derived from Digisonde vertical ionogram measurements. Figure adapted from [Reinisch, 2018].

The period of the height variation seen in figure 2.8 appear to be around 90 minutes, indicating a large-scale TID.

The motivation for studying TIDs is multifaceted. There is strong interest in the relationship between AGWs and TIDs because of the part they play in energy and momentum transfer between different regions of the atmosphere [Heitmann, 2020]. There is also interest in studying how TIDs affect the radiowave propagation conditions, as LSTIDs can cause variations in the maximum usable frequency (MUF) of more than 1 MHz [Verhulst, 2017]. This may affect radiowave communication or early warning defence systems, which provide further motivation for understanding and monitoring TIDs. Monitoring systems have been implemented, such as TechTIDE warning and mitigation services, which uses real-time data collected by ionosondes, HF Doppler systems and GNSS receivers to detect signatures of TIDs in real time [Belehaki, 2020]. The authors associated with TechTIDE are also participating in the Net-TIDE project, in which a network of synchronized oblique ionosondes are used to detect and analyze TIDs. The network utilizes bistatic oblique sounding between various locations in Europe, employing Digisonde DPS4D ionosondes to provide measurements of Doppler frequency, angle of arrival and time of flight [Verhulst, 2017]. There are conceptual similarities between the Net-TIDE project and the HF receiver we have developed for use in NOIRE. Details on the system requirements and design is provided in the next section.

/3

Design

The goal of this thesis project is to design and build a relatively low-cost radio receiver that is capable of listening to over-the-horizon radio transmissions and operate in a network. Designing such a system includes identifying the requirements and making a plan for fulfilling these requirements in order to ensure that the final device fulfills its intended purpose. The choices made for the design and the design process will be described in this chapter.

3.1 Design requirements

Frequencies and operation in a network

With this radio receiver system, we are interested in listening to over-the-horizon radio transmissions. A typical range of frequencies used for over-the-horizon radio transmission is 3-30 MHz, as electromagnetic waves of these frequencies can be reflected by the ionosphere. This frequency range is commonly called the *high-frequency* range. Waves of frequencies higher than 30 MHZ will normally not be reflected by the ionosphere. Waves of medium frequencies (0.3-3 MHz) suffer considerable absorption as they travel through the atmosphere in the day time [Davies, 1965], although reception down to 1 MHz is possible.

Additionally, the 4 radar receiver systems that will be constructed will be listening for over-the-horizon transmissions from a specific ionosonde transmitter located in Sodankylä, Finland. The transmitter, operated by Sodankylä Geophysical Observatory, is a Alpha-Wolf ionosonde [SGO, 2019]. The transmitter sweeps over the frequency range 0.5-16 MHz with a sweep time of roughly 30 seconds and a chirp-rate of 500.0084 kHz/s. The operational frequencies of the transmitter as well as the frequencies that will physically be able to reflect off the ionosphere will impact the choice of components for the system. We have therefore focused on the frequency range 1-30 MHz for this radar receiver system.

The radar receiver system is created with the sub-goal of it being able to serve as part of a larger network of radar receivers working together. In order to achieve this, the radar receiver must be equipped with the appropriate functionality for communicating and synchronizing with the network. This design will use GPS timing. Another sub-goal for this radar receiver system is that it could be used for investigating TIDs. As discussed in section 2.4, this puts some requirements of the sampling frequency. We have chosen to collect an ionogram every 1 minute, which is sufficient to fulfill the Nyquist sampling criterion when we take an approximate lower limit for the buoyancy period seen in figure 2.7 to be 5 minutes.

Cost, availability and open source software

Another sub-goal is to minimize the costs of manufacturing such a radar receiver. The intention is to be able to use this radar receiver design to populate a geographically distributed network of ionosonde receivers as part of the NOIRE initiative. Being able to procure relatively low-cost receivers is therefore desirable, as a lower cost means higher probability of being able to fund more receiver devices in more locations, improving the resolution of the envisioned network. A parts list of vendors used and approximate costs is included in appendix C. The design and implementation of the system also aims to use readily available components that anyone will be able to acquire or manufacture. This will be reflected in the simplicity of the design. It also relates to the fact that the software used to operate the radar receiver system is open source and accessible through the popular source code management site GitHub. The idea behind this is to enable users to modify and extend the functionality of the software to fit their own requirements.

Environment

The radar receivers will be deployed in the Fennoscandian region, were the climate is similar to that of the Arctic. This means that the radar receiver system needs to be weatherproofed and able to sustain temperatures below -30° Celsius. It must also be adapted for accumulation of considerable amounts of snow, in order to avoid mechanical failure from snow load. Another consideration is proofing against ice jacking.

3.2 System requirements

A radio receiver is a device that is capable of receiving a radio wave and extracting the information carried by the wave. The radio wave is received by an antenna (the driven element), a conducting structure of metal. Interaction with electromagnetic waves (radio waves) will induce a small alternating current in the antenna. This current constitutes a rather weak signal, necessitating a pre-amplifier in order to amplify the signal to usable power. To record the signal, the amplified signal must be passed through appropriate electronic circuitry in order for the signal to be presented to a computer in a usable form. This includes filtering to remove unwanted frequencies from the signal. The following section describes the solutions chosen for these segments of the over-the-horizon radio receiver system.

Antenna

This section discusses the design of the antenna. For the driven element, a magnetic loop antenna was chosen. In a regular dipole antenna, the electric field component of an incident radiowave induces a current in the conducting material. In a loop antenna, it's the magnetic field component that induces the current in the antenna. The magnetic loop antenna is compact and directional, but a central aspect is the fact that there is access to very cost-effective pre-amplifiers that have been made to work with magnetic loops. The loop antenna serves as an alternative to the traditional dipole antenna. If the loop parameters are selected carefully, the magnetic loop antenna radiation pattern is similar to the figure-eight pattern of a dipole [Balanis, 2016]. Assuming uniform current density, the radiation pattern changes with the the ratio between the loop circumference C and the wavelength λ of the incident wave. For loops of circumference smaller than 3.83λ the figure-eight shape is preserved. If this limit is exceeded, side lobes will develop in the radiation pattern. This is illustrated in figure 3.1. The equivalent limit for the radius is $R = 0.61\lambda$.

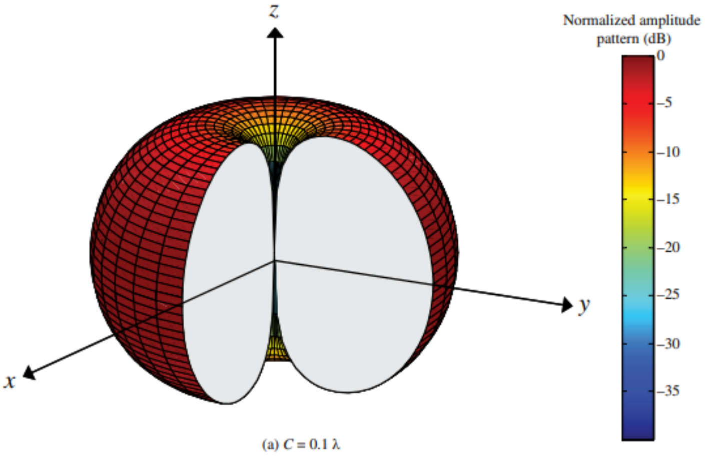

(a) $C = 0.1\,\lambda$

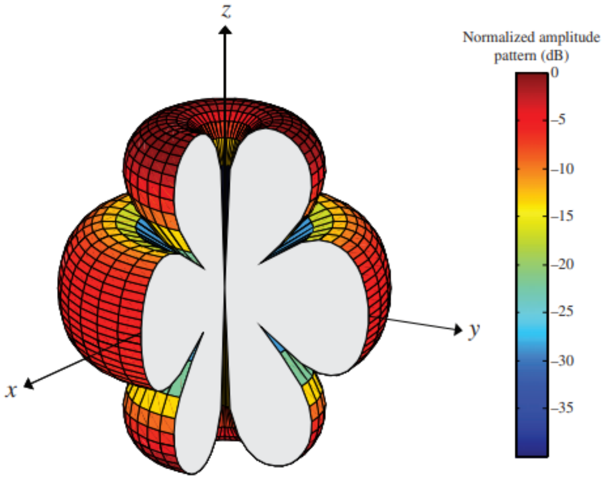

(b) $C = 5\,\lambda$

Figure 3.1: Radiation pattern depends on the circumference relative to the wavelength. For $C < 3.83\lambda$ the figure-eight pattern is preserved as in a), while for $C > 3.83\lambda$ side lobes forms as in b). The magnetic loop plane would be coincident with the xy-plane in this illustration. Plot adapted from [Balanis, 2016].

This means that if we want to achieve the figure-eight pattern, we must constrain the size of our loop to prevent sidelobe formation. Looking at the frequency range of interest, 1-30 MHz, and applying the relation $f = \frac{c}{\lambda}$

$$f_{min} = 1 \text{ MHz} \implies \lambda \approx 300 \text{ m}$$

$$f_{max} = 30 \text{ MHz} \implies \lambda \approx 10 \text{ m}$$

This means that as long as the radius of our magnetic loop is below $r_{max} = 0.61\lambda = 0.61 \cdot 10 \text{ m} = 6.1 \text{ m}$, we will avoid the sidelobe formation. Using an antenna of radius $r \approx 56$ cm (the radius of a loop antenna with 1 m^2 collecting area) will therefore require less material for the loop, reducing the total weight and cost of the antenna segment. This is the radius that is chosen for this project and it will also keep the antenna compact enough to be transported by a car. With the figure-eight pattern it is also possible to use the directional property of the antenna to maximize the gain in the direction of signal arrival. As for the material of the loop, aluminum is chosen due to being a lightweight yet rigid material that also has good electrical conductivity.

The aluminum loop will be elevated above ground to improve line-of-sight by mounting it on a support mast that is non-conductive to avoid electrical interference. Fiberglass is not conductive and exhibits rather high rigidity, making it a suitable material for a mast to support the loop antenna. If the mast is hollow it should be mounted in such a fashion to allow for water drainage, avoiding ice jacking cracking the mast. Usually, the effects of the ground will have to be considered in antenna designs, as it will serve as a conducting plane that will reflect the radiowaves and possibly interfere with the signal. This is usually counteracted by elevating the antenna above ground, but for vertical loop antennas the effects of the ground plane are minimal.

It is also necessary to design a mast mount for the antenna element. This should be a simple pole mount that will fix the antenna element to the mast, and should also have space for mounting the pre-amplifier onto it. A low-cost pre-amplifier has been pre-selected for this design, motivated by the desire to minimize the cost. This is the variable gain MLA-30+ pre-amplifier, which will be described in more detail in the implementation chapter. As such, the mast mount must be designed to accommodate this type of pre-amplifier.

Software defined radio

Encoding information into a radiowave involves some form of modulation. Radiowave modulation entails varying the certain properties of the periodic wave. Typically the properties used for modulation are frequency, amplitude or phase. Having controlled alteration of these properties allows for information to be encoded into a transmission. Before the digital age, modulation was achieved by installing or removing specific hardware components in a radio communications system (such as amplifiers, switches and filters). As can be imagined, this is quite laborious. In the modern day we have access to a flexible set of hardware components that enable the alteration of the wave properties by using software programs to implement the same functionalities as was previously achieved by using analogue techniques. This is known as a software defined radio (SDR), and together with a computer it handles the signal processing. This design will employ an SDR device from one of the product lines manufactured and sold by Ettus Research. More detail on the specific device is given in the implementation chapter.

Electronic circuit and computer

The design must also address the necessary electronic circuit and the operating computer. If this build was designed a hundred years ago, there would have been a sizeable portion of electronics to select and configure in order to be able to receive the signal of interest. Luckily for us, the SDR will handle most of it in this build. There are still some electronic components that require selection. These mainly include a low-pass filter between the pre-amplifier and the SDR, as well as a means of powering the pre-amplifier. The MLA-30+ comes bundled with a bias-tee, which is a three-port device that enables both pre-amplifier powering and signal transmission on the same cable. This lets the pre-amplifier be powered by DC without interfering with the RF signal. The bias tee, powered by USB connected to the computer, should be connected somewhere between the pre-amplifier and the SDR.

The design also necessitates a computer, which will interface with the SDR, perform calculations involving the collected data and upload data to an accessible server. To contribute to a smaller footprint and also make it easier to contain all the electronics within an enclosed space, a small form factor computer is desired. The computer must have at least 64 GB of RAM and 500 GB of drive storage in order to handle all the data, as well as an internet connection. The computer must also be set up for remote access, to avoid travelling to each site to make adjustments to the software. In addition, the computers must also be set up with some networking protocol in order for the computers in the network to be synchronized. All the electronics should also be contained within an enclosed space for easier transportation and a cleaner install at each site. The cable connecting the antenna to the enclosed case will need to be a robust type of coaxial cable, and with a length of 80 meters in order for the antenna to be installed a distance from the other experiments on the sites.

3.3 Visualization of the antenna design

A computer-aided design (CAD) program was used to visualize the design of the antenna element and mast solution in the form of 3D models. The CAD-program was SolidWorks 2021/2022 edition used with a student license generated by the university. Disclaimer: I am not a professional technical draftsman, meaning that the CAD models are likely not up the industry standard of technical drawing. The intention behind the 3D modelling is to visualize the design prior to implementation and communicate the design ideas. Images of the CAD models can be seen in figure 3.2. The CAD files in original SolidWorks formats (.SLDPRT and .SLDASM) can be found here: `https://github.com/jflob/receiver_antenna_CAD`.

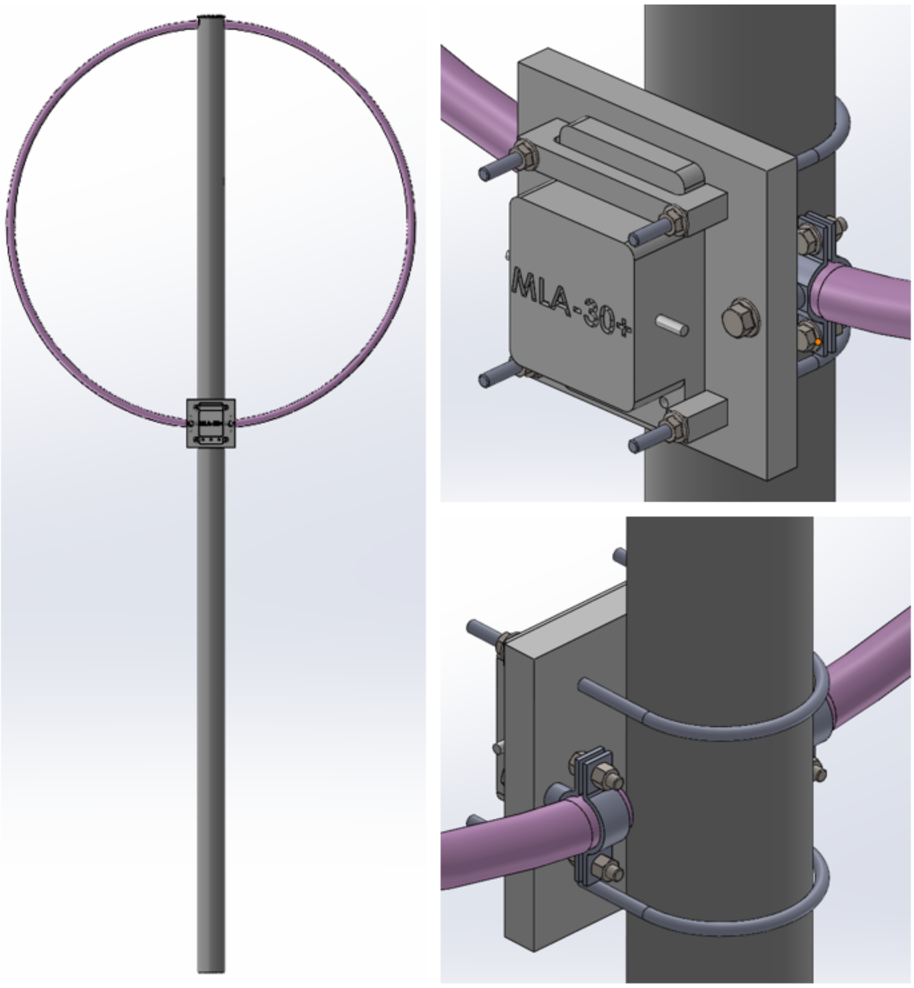

Figure 3.2: Images of the CAD models of the antenna design. Full frontal view (left) showing the top segment of the antenna design. Rear isometric view (bottom right) showing the rear side of the mast mount and how it the mount is fastened to the mast. Frontal isometric view (top right) showing the front side of the mast mount where the pre-amplifier is mounted.

Schematics

With the design requirements and some design choices laid out, providing a schematic is helpful in communicating the design. The schematic in figure 3.3 shows all the electronic components and antennas involved and how they are connected.

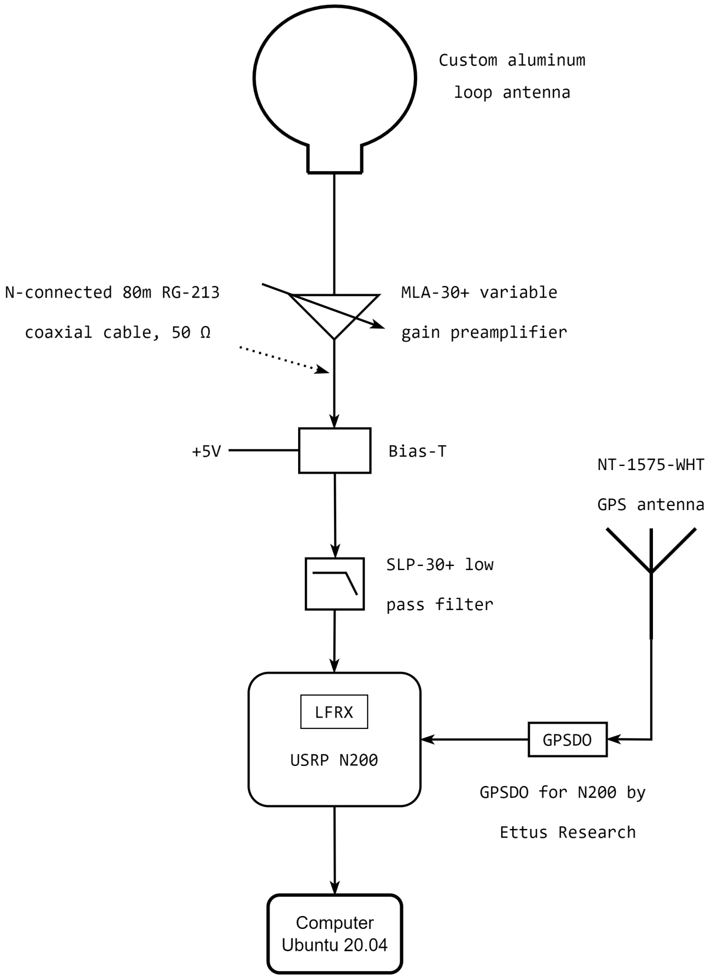

Figure 3.3: A schematic showing the different segments of the radar receiver as well as how they are connected.

4

Implementation

This chapter concerns the implementation of the design. Implementation is the step in which an idea or a design is realized into a physical system. The chapter will cover the solutions and components that were chosen in order to fulfill the demands of the design. In appendix C a parts lists with prices can be found.

4.1 Mast

The material for the mast that will suspend the driven antenna element was chosen to be fiberglass tubing of inner diameter ø59 mm and outer diameter Ø66 mm. These tubes were purchased in lengths of 2.38 m from company Eidolon AS, of which two lengths were joined to form the mast. The two lengths are joined by a machined aluminium joint, made to run inside the fiberglass tubing. An example of the joint can be seen in figure 4.1.

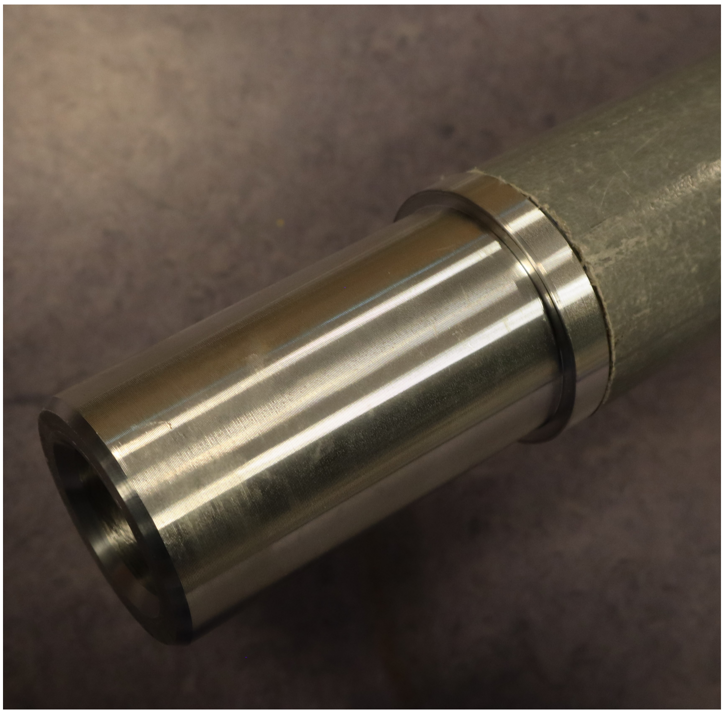

Figure 4.1: An image showing how the two lengths of fiberglass tubing that constitute the mast is joined using an aluminium joint running inside each tube segment.

The aluminium joint simply slides inside each segment of tubing. There are no lock screws or other fastening methods, instead the joint relies on being "activated" by some downwards pull on the top tube segment. This is partially achieved using the force of gravity, but also by attaching four guy-wires to the top segment and running them to either a nearby tree or a tent pole driven into the ground. These guy-wires also serve to stabilize the entirety of the antenna system, and their attachment points at the top tube segment are some threaded rods running through the tube with screw-on rings on both sides. This can be seen in figure 4.2, which also displays the type of tent pole used. The guy wires themselves are simple, synthetic rope. This is then tied to the ground anchoring points on one end, and then tied to a rubber-loop running through the on-mast anchoring points on the other end. The idea is that the flexible rubber-loop will help keep tension on the guy-wire.

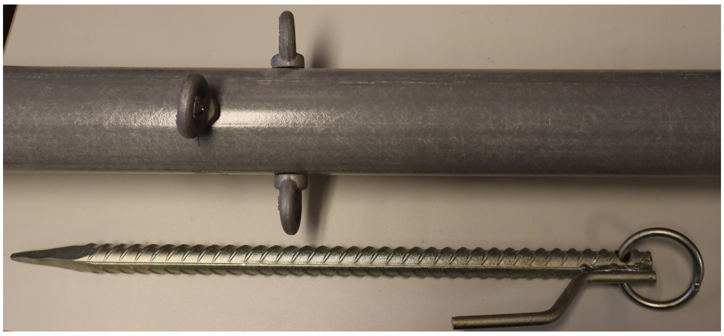

Figure 4.2: An image showing how the top tube segment of the mast is equipped with rings for guy-wire attachment. The image also show the tent pole used for attaching the guy-wires to the ground.

Lastly, the bottom tube segment is bolted onto an earthen anchor (originally designed for fence post installation). The earthen anchor is a 0.75 m spike that is driven into the ground using a sledgehammer prior to bolting the bottom tube segment onto it. A piece of wood is used between the anchor and the sledgdehammer to avoid deformation of the sheet metal. A photo of the anchoring can be seen in figure 4.3.

Figure 4.3: An image demonstrating how the bottom tube segment will be bolted to the earthen anchor after it has been driven into the ground (left). Using a sledgehammer, the anchor is driven far enough into the ground so that only the square part of it is revealed (right).

4.2 Pre-amplifier MLA-30+

An inexpensive pre-amplifier with variable gain by model name **MLA-30+** was selected to address the systems need for signal pre-amplification. This device was selected due to its low cost, weather-proofed housing and active frequency range of 100 kHz-30 MHz. The stock MLA-30+ is equipped with an SMA-cable connecting the pre-amplifier to the receiving electronic circuit and a 2 mm thick aluminium wire that serves as the driven element of the antenna. The MLA-30+ also comes equipped with an USB-powered bias tee used for powering the pre-amplifier. The bias tee is also responsible for separation of the DC power component and the signal. In order to address the needs imposed by the harsh operation climate, both the cabling and the driven element were subjected to modification. The SMA cable, previously run through a simple bore in the housing, was replaced by a bulkhead N connector mounted on the housing, enabling the use of the much more robust RG-213U coaxial cable. In figure 4.4 both the unmodified and modified pre-amplifiers can be seen.

Figure 4.4: An image showing the pre-amplifier as a stock MLA-30+ (right) and the modified MLA-30+ (left).

The modification of the pre-amplifier started by removing the epoxy-coated (the coating is applied by the manufacturer for weather-proofing) circuit board inside the pre-amplifier housing. This was done by unscrewing a screw only accessible by removing some of the epoxy coat. When the circuit board was loosened, the SMA cable was cut and the board removed. As the N connector that will be fitted is much bulkier than the stock solution, more space inside the housing was needed. This was achieved by removal of a couple plastic suspension brackets inside the housing, as shown in figure 4.5.

Figure 4.5: The plastic suspension brackets inside the housing were removed to clear more space for the N connector.

According to the specification provided together with the N-connector, installation requires a ø16 mm hole, which was promptly made in the housing using a drill and a dremel. The result can be seen in figure 4.6.

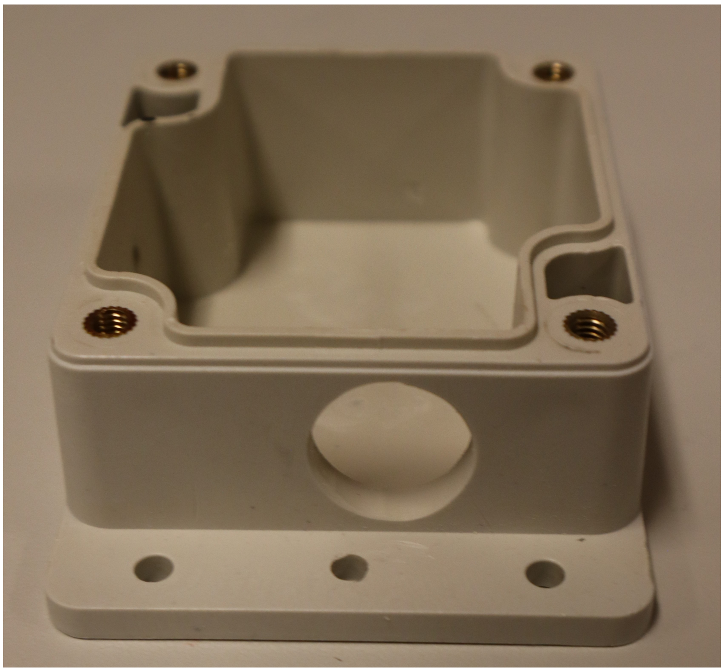

Figure 4.6: Drilled a hole in the pre-amplifier housing for mounting the N connector.

It was also necessary to modify the circuit board inside the pre-amplifier. The SMA cable that was previously running through the housing was coupled directly onto the output of the electronic circuit, enabling us to reuse it with the N connector. The SMA cable was stripped in order to attach it to the N connector. This was done by soldering the center terminal of the N connector onto the SMA cable core while making sure the shielding was in contact with ground. The result can be seen in figure 4.7.

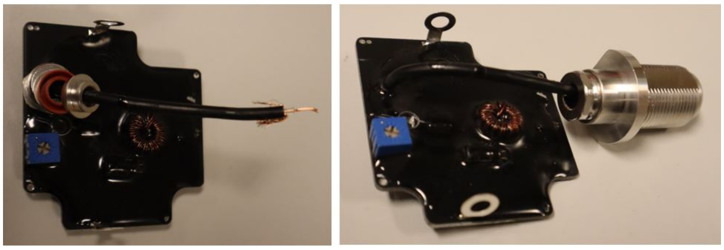

Figure 4.7: The pre-amplifier circuit board. The attached SMA cable is stripped and the cable core is soldered onto the center terminal of an N connector.

Inserting the circuit board and the N connector back into the housing, the N connector was fixed in place with the accompanying washer and nut, and the pre-amplifier housing was sealed by reattaching the lid. The pre-amplifier modification is complete, and the pre-amplifier now takes form as seen in figure 4.8. In this complete state the pre-amplifiers were bolted onto the mast mount.

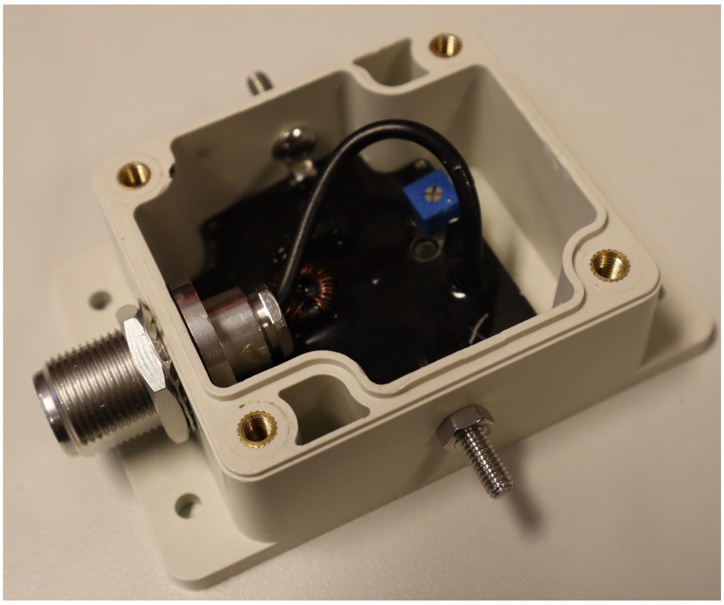

Figure 4.8: The complete modified pre-amplifier, as it was used in the finished systems.

The MLA-30+ comes equipped with a USB-driven bias-tee for powering the pre-amplifier, which was used for said purpose. The bias-tee can be seen sitting on top of the radio receiver in figure 4.17, where it is connected to the antenna/pre-amplifier, the receiver and by USB to the computer for power.

4.3 Driven element and mast mount

Originally in the stock version of the MLA-30+ preamp, the driven antenna element was a thin aluminium wire. In this build, the driven element was upgraded to Ø20 mm aluminium tubing mounted using pipe-clamps and bolts, as a more sturdy construction will have a higher chance of surviving the arctic climate the instrument will operate in. The collection area of the aluminium loop is 1 m^2, corresponding to a diameter of approximately 1.13 meters. The aluminium loop was attached to the very top of the fiberglass mast. This was achieved by creating grooves in the tube end, as well as locking it in place with a screw running through a lid on the top.

The two open ends of the aluminium loop must be coupled to the terminals of the modified pre-amplifier, and the subsystem this constitutes must be fixed to the antenna mast itself. A mast mount was commissioned from the university workshop. The mount is a square piece of plastic onto which both the pre-amplifier and the aluminium loop are fixed. The mast mount is fixed to the fiberglass mast using two U-bolts made out of threaded rods. These U-bolts run through the mast mount plate and are fastened with lock-nuts sitting on top of some spacers. The spacers create needed space for the pre-amplifier, as the U-bolts protrude through the front side of the plastic holding bracket. The pre-amplifier is bolted in place on the front side of the instrument, while the aluminium loop is fixed by bolting a pair of aluminium tube clamps onto the backside of the plastic holding bracket. This can be seen in figure 4.9.

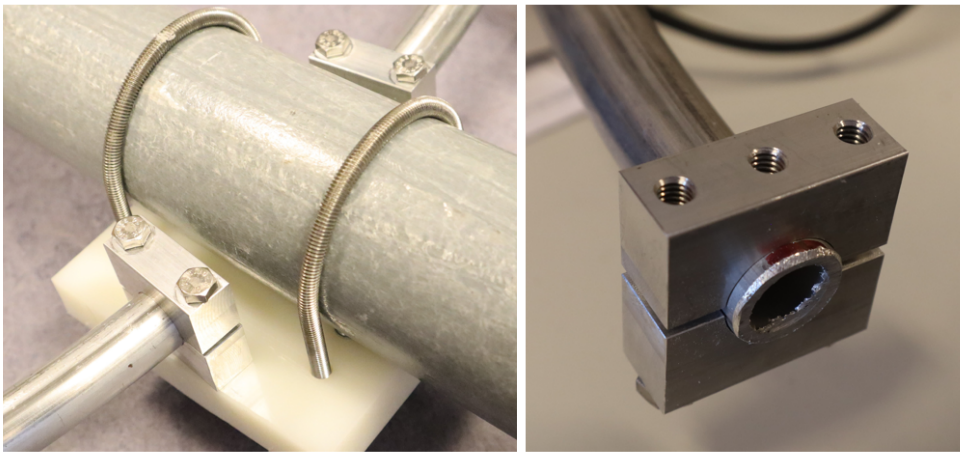

Figure 4.9: Mast mount solution with tube clamps. Clamps manufactured by Yngve Eilertsen of the UiT mechanical workshop.

The driven element must be connected to the terminals of the pre-amplifier. This was achieved by cutting some short lengths of wire, whose ends were outfitted with crimped cable lugs. The cables were then insulated using heat shrink tubing, and connected to the pre-amplifier terminals on one end while being connected to a bolt running through the aluminium tube clamps. The cable constituents, the finished cable and the connected cable can be seen in figure 4.10. Electrical connection between each terminal and any point on the driven element was measured and confirmed using a multimeter.

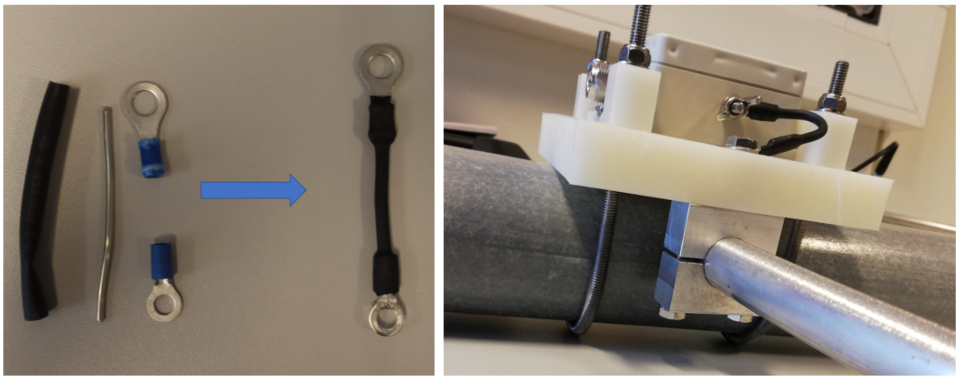

Figure 4.10: Cables with crimped cable lugs are connecting the pre-amplifier terminals to the driven element through the tube clamps.

A larger image of the magnetic loop element, the mast mount and the fixed pre-amplifier can be seen in figure 4.11.

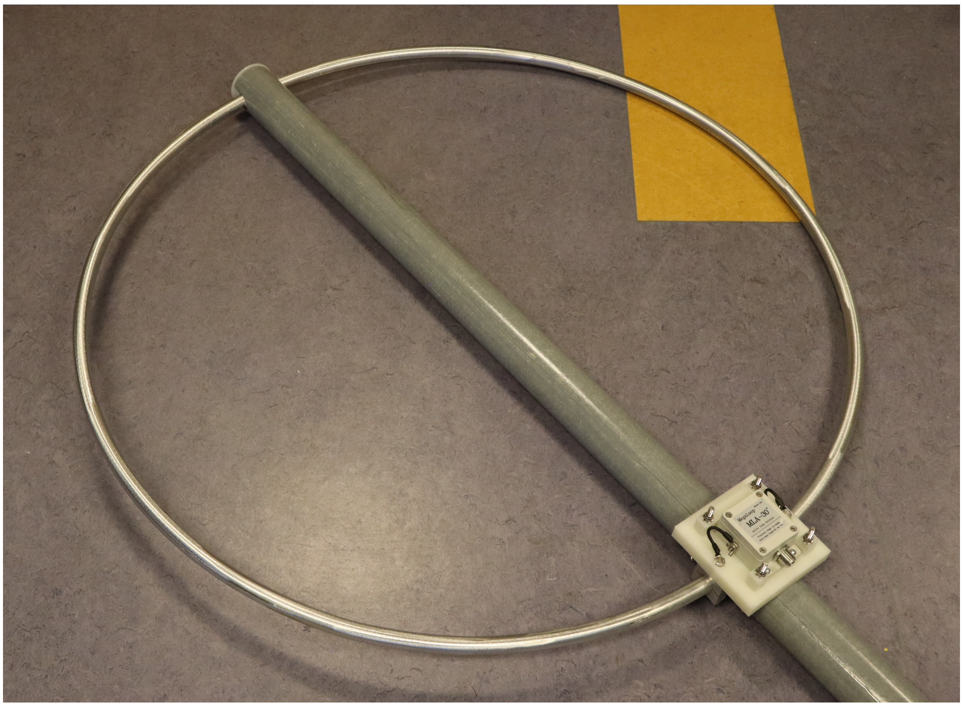

Figure 4.11: The complete solution for the antenna element and mast mount.

4.4 Software defined radio - USRP N200

The company Ettus Research develops and sells a series of software defined radio devices in their brand series **U**niversal **s**oftware **r**adio **p**eripherals, or USRP. Each of these devices is supported by the USRP Hardware Driver software, UHD, which is open source and developed by the same company. One of these devices is the USRP N200, which is the chosen SDR device for this build. The USRP N200 can be seen in figure 4.12.

Figure 4.12: The USRP N200 software defined radio used in the project. Image retrieved from manufacturers webpage: `https://www.ettus.com/all-products/un200-kit/`.

The USRP N200 is marketed as a high performance SDR device offering flexibility, great bandwidth and dynamic range. More information on the device itself can be found in the datasheet [EttusResearch, 2022b]. The USRP N200 is designed in a modular fashion, allowing the user to modify its functionality by installing various types of daughterboards. For the application of this ionosonde receiver, modules for receiving RF signals and synchronizing through GPS was needed.

As we already have an external low-noise amplifier (the MLA-30+ preamp) and the signal is filtered prior to reaching the N200, the LFRX daughterboard was selected to get direct access to the ADC inputs with low-pass filtering. The LFRX daughterboard is designed to receive signals from DC to 30 MHz. A photo of the LFRX being installed on the motherboard of the N200 can be seen in figure 4.13.

Figure 4.13: LFRX daughterboard being installed in the N200.

We also needed to install a GPSDO. A GPS **d**isciplined **o**scillator (GPSDO, also known as a GPS clock), is a GPS receiver in combination with a high-quality crystal oscillator that is used to keep track of time. The GPSDO is configured to be in agreement with the accurate time signals broadcasted by GPS satellites. The satellite signal is received by an active GPS antenna connected to the GPSDO installed in the N200 device. Ettus Research provides a GPSDO kit specifically made for the N200/N210 series, which was selected for use in the instrument. The GPSDO module was installed in accordance to the installation instructions [EttusResearch, 2022a], and the installed module can be seen in figure 4.14.

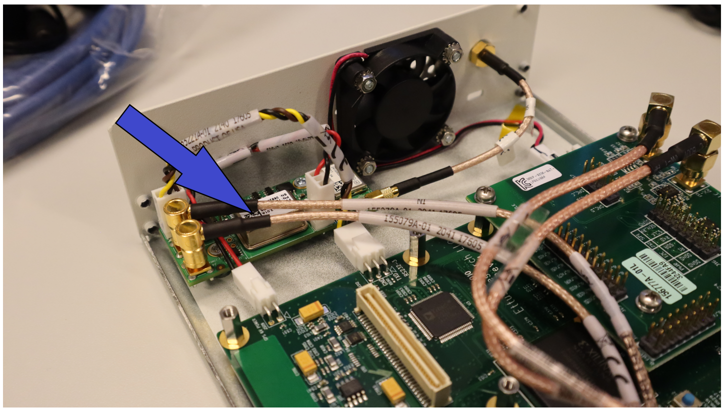

Figure 4.14: GPSDO module installed in the N200.

4.5 Computer

Sticking to the intention of using a small-form factor computer when building the radar receiver instrument, we purchased ASUS MINIPC PN51 computers to operate the software and communicate with the USRP N200. A photo of the PN51 can be seen in figure 4.15.

Figure 4.15: ASUS MINIPC PN51 computer used in the instrument. Image retrieved from manufacturers webpage: `https://www.asus.com/Displays-Desktops/Mini-PCs/PN-PB-series/Mini-PC-PN51/`.

The computers were equipped with 64 GB of RAM and either a 1 TB or 500 GB SSD disk for storage. The large amount of RAM (relative to the disk space) is needed for the raw complex voltage recording, which is then processed into ionograms with smaller memory footprint. The ionograms are of size 0.4 MB, one of which is produced at the receiver each minute. Communication between the N200 and the computers occurs via 1 Gbit Ethernet cable. The computers also use a cabled Ethernet connection (via a USB to Ethernet adapter) to access the internet. The Linux operating system Ubunutu 20.04 LTS was installed on all the computers, as this is the operating system that the software was tried and tested on. The networking protocol was also set up on all the computers. We first tried the traditional NTP networking protocol, but we couldn't achieve a tolerable clock synchronization correction with the NTP servers. Instead we configured the *chrony* protocol available for Ubuntu systems [Lichvar, 2021], which achieved sufficient clock accuracy.

4.6 Rack mounted case

Containing all the electronic components and circuits inside an enclosed space will make the installation cleaner and contribute to keeping the sites for deployment tidy. A rack mounted case was acquired from RS Online to serve as the vessel for the receiver circuit and computer. The rack mounted case, model RS PRO 3U, measures 133 mm x 483 mm x 466 mm and comes with perforated side panels for ventilation. The USRP N200 radio and the industrial mini-PC is contained inside the case and fastened to the bottom panel using velcro-tape. Panel-mounted bulkhead adapters were installed on the front plate of, ensuring clean cable routing from outside to inside the case. As seen in figure 4.16, the following panel adapters were installed:

- A female-female SMA adapter for the GPS antenna cable
- A female-female N-SMA adapter for the coaxial signal cable from the pre-amplifier
- A female-female Ethernet port for establishing a wired internet connection

Figure 4.16: Bulkhead panel adapters installed in the front plate of the rack mounted case, labelled.

In figure 4.17, the rack mounted case with all its content installed can be seen. This includes the USRP N200 and the black small-form computer. Inside the case is also various cabling, a cylindrical SLP-30 low-pass filter and the bias-tee used for powering the pre-amplifier. The next paragraph will detail the solutions for powering the case.

Figure 4.17: Overview of the rack mounted case with installed components.

Powering the case

As both the USRP N200 and the computer need 230V power, various solutions were tried for powering the rack mounted case. The first attempt was running a power cable through a feedhole in the front plate, attached to a multi-socket inside the case. However, this proved to be a safety concern as the cable insulation could be worn out over time and expose the live wires. This solution was scrapped in favor of installing C14 panel mount adapters in the front plates, as shown in figure 4.18.

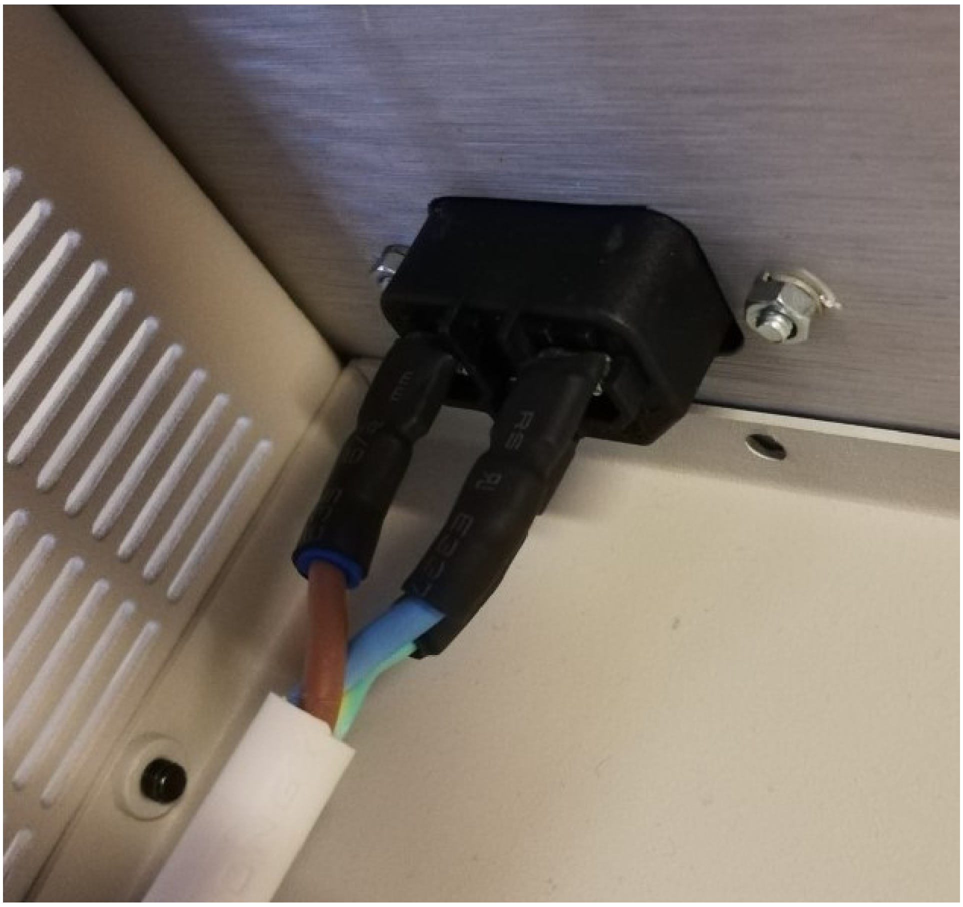

Figure 4.18: Panel mounted power adapters.

This is a clean looking solution, but when we arrived in Finland to do the installations, there were still concerns about the safety. The ground of a panel mount of this type was floating, meaning that this solution for powering the case was not accepted in the Finnish electrical safety code. In the end, the multi-socket was moved outside the case entirely. The power transformers for the N200 and the computer were moved outside the case as well, meaning that only the thin wires bringing low-voltage to the electronics were being fed through the front plate (see figure 4.17). This way the voltage in the power cables running through the front plate was only 6V as opposed to 230VAC. This was within the requirements of the electrical safety code and was subsequently the applied solution. There was one case (installed in the Kuusamo site) were the C14 solution was modified to be properly grounded to Earth with a panel mount adapter provided on site.

4.7 GPS antenna

The GPS antenna used in this radar receiver is a Mobilemark NT-1575-WHT, operating with frequency 1575 ± 2 MHz. The GPS antenna is shown in figure 4.19, where it can be seen mounted on an L-bracket for wall mounting. Also seen is the 10 meter male-male 50 Ω TNC-SMA cable used to connect the GPS antenna to the rack mounted case. The heavy duty antenna is shaped like a dome to avoid build-up of snow, and is designed with the operating temperature range -40°C to +80°C. More information about the GPS antenna can be found in the manufacturers manual [Mobilemark, 2022].

Figure 4.19: Mobilemark NT-1575-WHT antenna with 10 meter coaxial cable.

4.8 Software

The radar receivers operate using a software suite developed and implemented by Juha Vierinen. The software is open source and available to anyone through

GitHub [Vierinen, 2022]. The software is used for detection of chirp sounders and reception of over-the-horizon radio transmissions, which it uses to calculate ionograms. It also ensures GPS-locking for synchronization purposes. Operating the software enables the user to both record and store the raw voltages induced in the magnetic loop antenna, but also to calculate and plot ionograms from the measured voltages. Figure 4.20 displays an activity diagram describing the *rx_uhd.cpp* program that records and stores raw voltage measurements. Notice how the program ensures GPS lock before proceeding with a measurement, in order to guarantee synchronization.

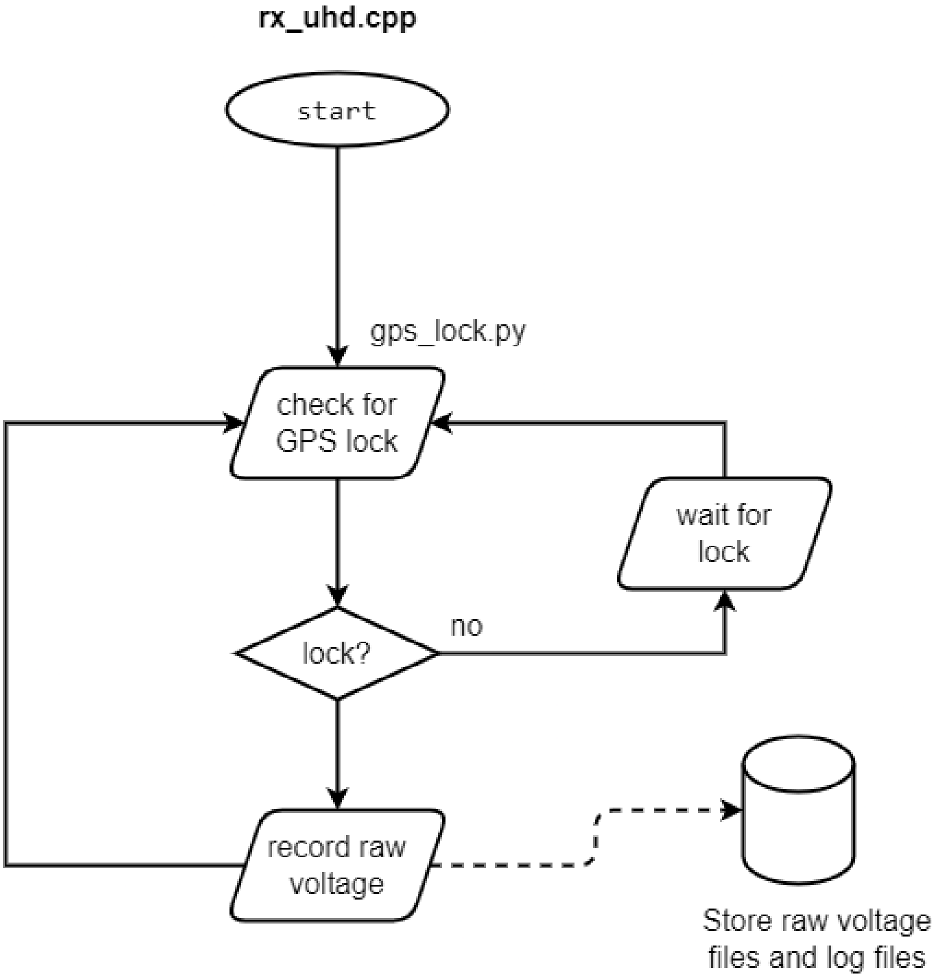

Figure 4.20: Activity diagram showing the process of leading up to recording and storing raw voltage data from the antenna.

As mentioned, the software also handles the calculation and plotting of ionograms. The activity diagram in figure 4.21 shows which software segments go into the process of calculating ionograms from the raw voltage data. This is also dependent on the GPS lock in order to ensure synchronization with the transmitter. This is also where down-conversion of the chirp signal occurs.

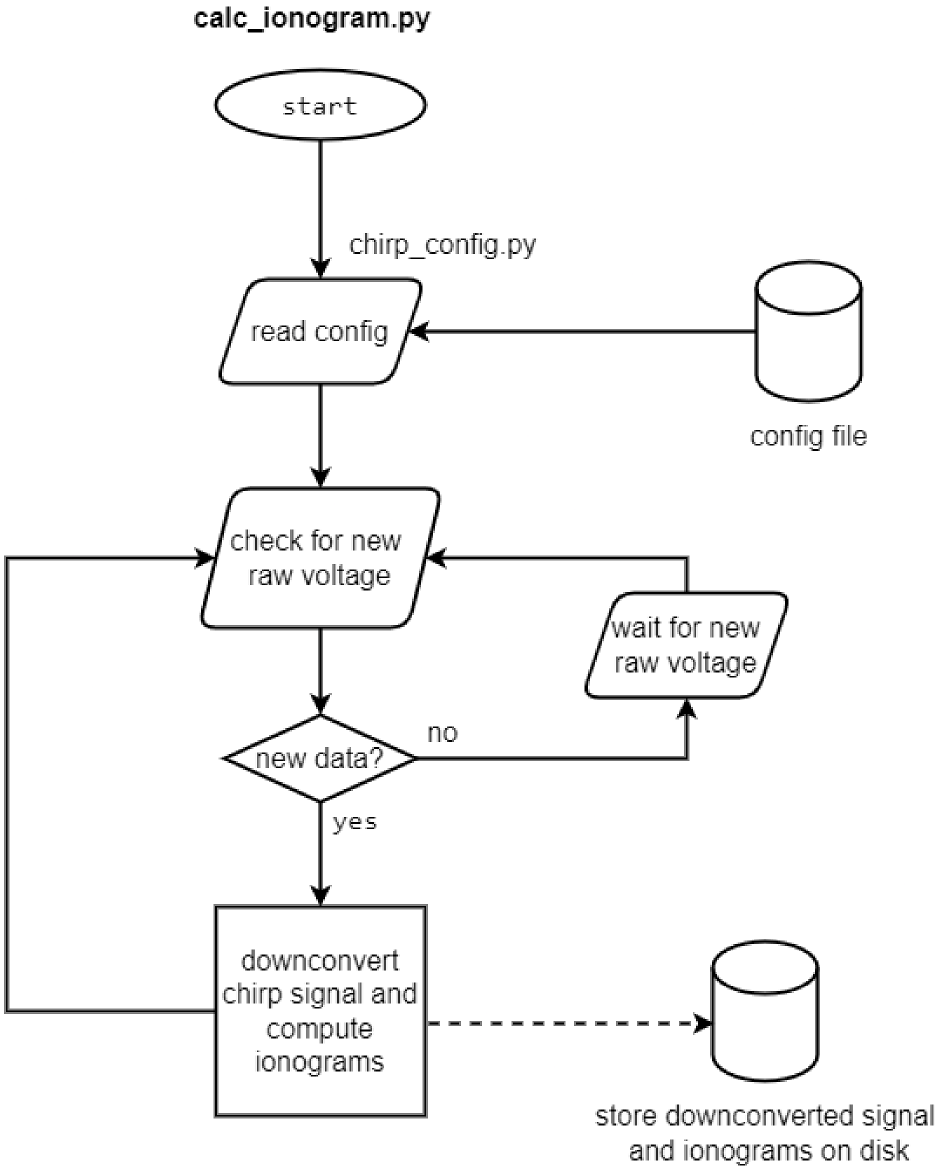

Figure 4.21: Activity diagram showing the process of producing ionograms from stored raw voltage data.

An activity diagram describing the plotting of the ionograms can be seen in figure 4.22. Similar to the *calc_ionogram* it also relies on the configuration file.

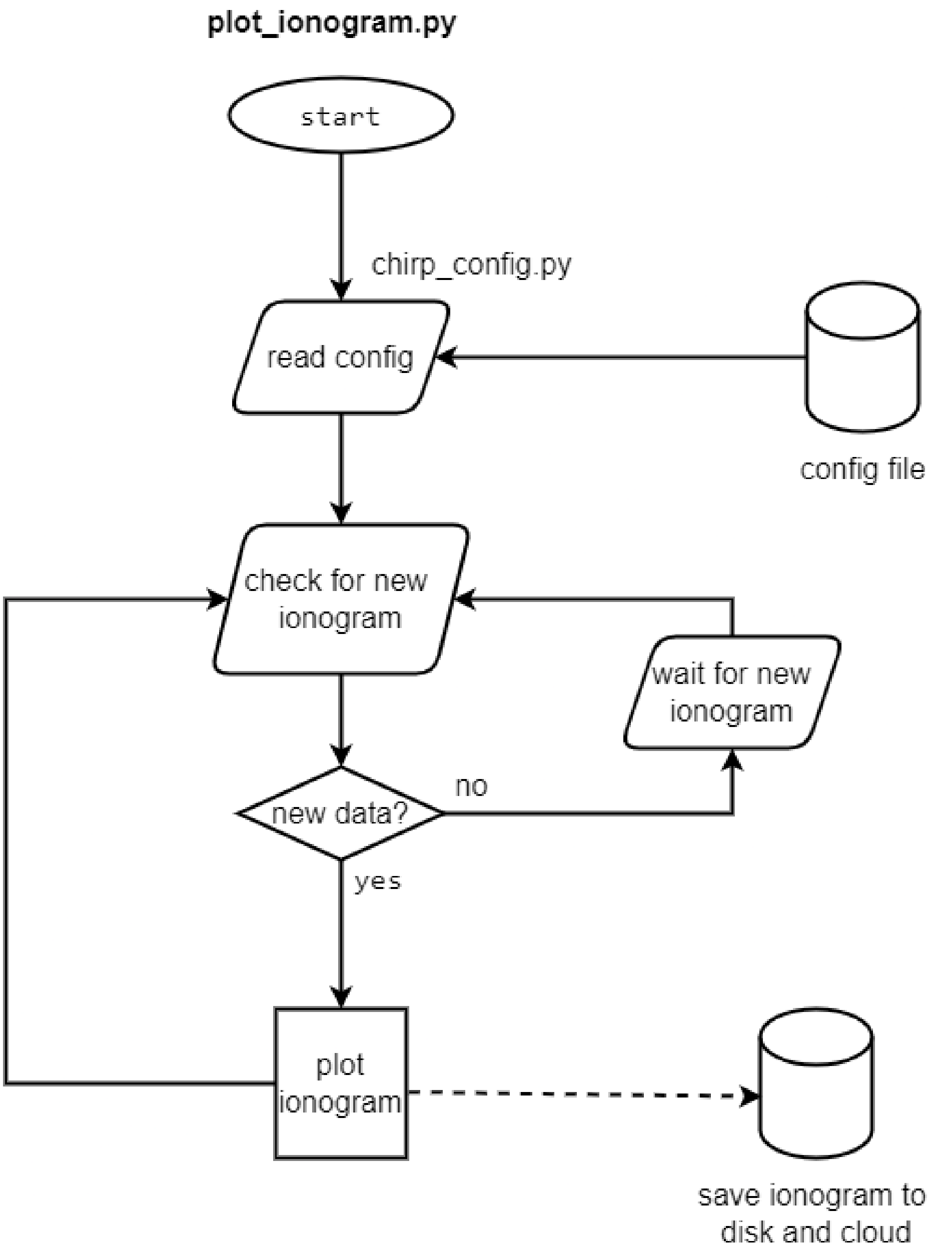

Figure 4.22: Activity diagram showing the process of plotting ionograms from stored calculated ionogram data.

4.8.1 Installing dependencies

The software is bundled together and can be found online on GitHub [Vierinen, 2022]. The full package software dependencies can be installed by running the commands given in the *dependencies.txt* file provided on GitHub. The file can also be seen listed in appendix A.

4.8.2 Making a measurement

If the assembled antenna system is deployed and the software suite has been set up according to *dependencies.txt*, a measurement can be made by running the *sgo.sh* shell script, which depends on the *sgo.ini* file for configuration. Both of these scripts are included in appendix A. The *sgo.sh* shell script will start all the necessary processes for making a data capture, examples of which include the processes displayed in figures 4.20, 4.21 and 4.22. In the GitHub repository [Vierinen, 2022] several shell scripts can be found, configured for the installation sites given by the file name (i.e. the name *sgo_ski.sh* indicates that the script is made for use with the Skibotn system etc.).

5

Laboratory testing

Prior to deployment, the radar receiver systems were set up and tested in a laboratory setting. The tests involved setting up the computers with all the necessary dependencies and ensuring that the remote access configuration was working before collecting some data and plotting a few sample ionograms. The first system we installed in Skibotn was installed before the day the other three systems were tested in the lab, meaning that the Skibotn was field tested and therefore the sample ionogram for the Skibotn system was collected in Skibotn. Prior testing with the Skibotn system was performed during development and assembly, with its field deployment serving as a dress rehearsal for the other installations. The other three systems going to Finland were subjected to testing in the laboratory before deployment.

Each system was named in series OTHRx, for **o**ver-**t**he-**h**orizon receiver:

- OTHR1 - Oulu system
- OTHR2 - Skibotn system
- OTHR3 - Kuusamo system
- OTHR4 - Ivalo system

The complete cases, with the content installed as described in the implementation chapter, were set up in the laboratory. Each system was in turn connected to the monitor, loop antenna and a GPS antenna for testing. The loop antennas and the GPS antennas were set up in a parking lot outside the laboratory building. The location is indicated on the map seen in figure 5.1.

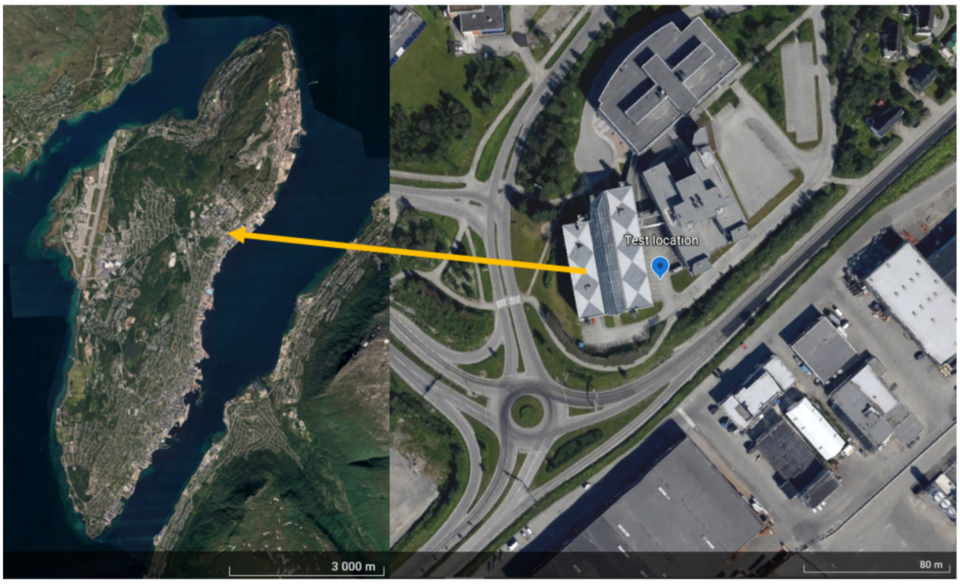

Figure 5.1: The location where the laboratory testing took place. The island seen in the larger scale image is Tromsøya, Norway.

After each system was accessed remotely by my supervisor, the data collection was started by running a shell script (configured to look for transmissions from Sodankylä with a chirp-rate of 500.01 kHz/s) that starts all the necessary software to configure the USRP and start collecting data. The software simultaneously tries to attain a GPS lock for timing. Once a lock has been achieved, collection of raw voltage data ensues. Once a capture is complete, the data is processed and an ionogram is plotted.

The parking lot where the systems were tested is located in the middle of a commercial area. This means that there are numerous sources for interference, such as power supply adapters, scientific instrumentation and powerlines. Despite this we were still able to successfully capture ionograms with reasonable signal-to-noise ratios for the Sodankylä echo traces, which can be seen in the following subsections.

The ionograms presented here use frequency in MHz on the x-axis and one-way range offset in kilometers on the y-axis, with the received power indicated in the color plot by signal-to-noise ratio in decibels. Travel time is typically seen on the y-axis in ionograms. The one-way range offset is related to the travel time because it represents the distance the wave has travelled for a single hop along a virtual travel path. Virtual path means that the path is approximated as a triangle spanning from the transmitter to the receiver, much like the one seen in figure 2.5. As discussed previously the wave path is in reality not triangular but rather shaped by the refraction the wave experiences as it travels. Similar to the virtual height being overestimated due to this idealization, so is the one-way range offset.

OTHR1 - Oulu

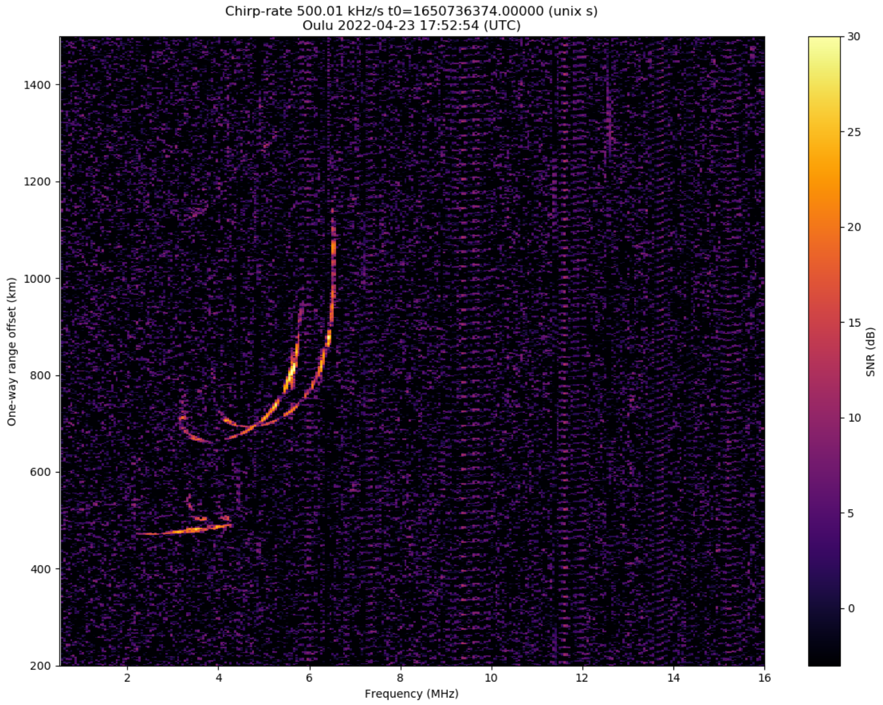

Figure 5.2: Sample ionogram collected with the OTHR1 radar receiver.

As can be seen in figure 5.2, we can clearly see the traces of the E-region around the one-way range offset of 500 km for frequencies 2-4 MHz. We can also clearly see the traces from the F-region spanning from a one-way range offset of around 700 km up to around 1200 km for frequencies 3-6 MHz. We can see the traces from both the ordinary and extraordinary wave modes in the F-region, with the x-mode trace being up-shifted in frequency as expected. The signal-to-noise ratio for the traces appears to be above 15 which is reasonable. The OTHR1 system appears to be fully functioning.

OTHR2 - Skibotn

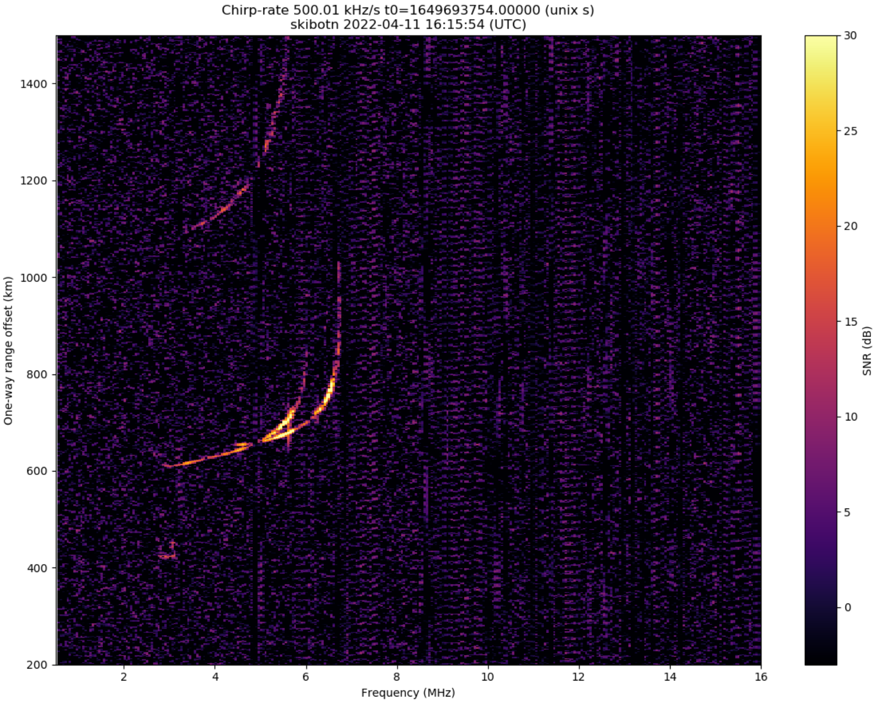

Figure 5.3: Sample ionogram collected with the OTHR2 radar receiver.

In figure 5.3 we can see a slight E-region trace around 400 km and 3 MHz. We can also see the traces for both o-mode and x-mode waves starting around a one-way range offset of 600 km and frequency 3 MHz. Visible in this ionogram is also the trace for what is likely a multi-hop echo starting around a one-way range offset of 1100 km and a frequency of 3 MHz. The signal-to-noise ratio attained seems sufficient, at least for the F-region traces. The OTHR2 system appears to be fully functioning.

OTHR3 - Kuusamo

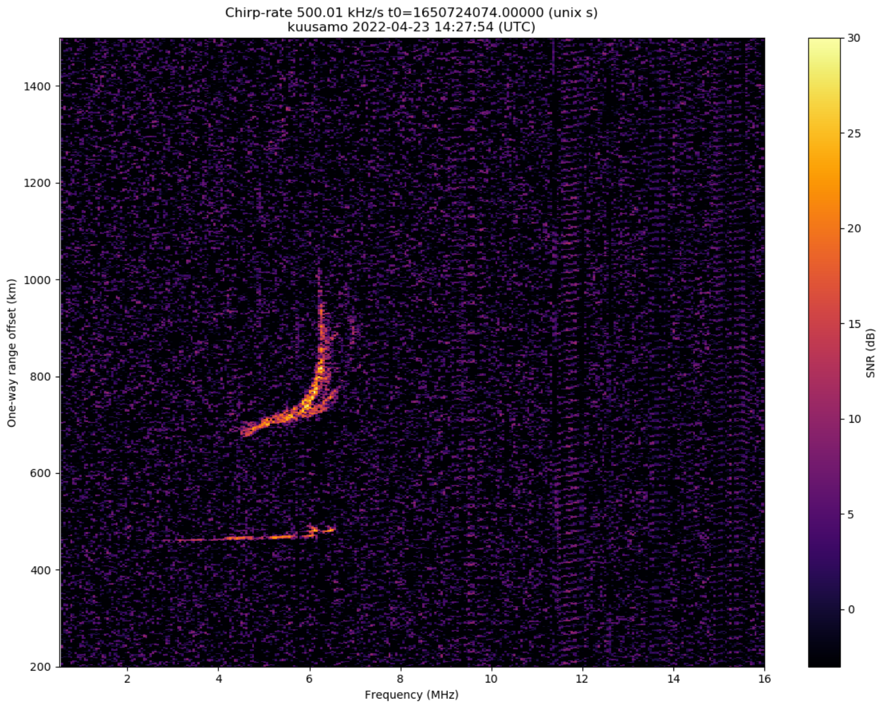

Figure 5.4: Sample ionogram collected with the OTHR3 radar receiver.

The ionogram that can be seen in figure 5.4 also exhibits traces from the E-region at one-way range offset 500 km and frequency 3 MHz, but in this measurement the trace extends to somewhat higher frequencies compared to the two previous examples. This might be due to sporadic-E. The traces from the F-region starting at a one-way range offset of 700 km and a frequency of 4 MHz appear to be somewhat smeared, making the shift in frequency between the o-mode trace and the x-mode trace less visible. The smearing is likely due to a phenomenon called spread-F. Spread-F are particularly diffuse F-region traces in an ionogram, caused by ionospheric structures with irregularities in density. This is correlated with magnetic activity [Perkins, 1973]. The signal-to-noise ratio is sufficient in this ionogram as well. The OTHR3 system appears to be fully functioning.

OTHR4 - Ivalo

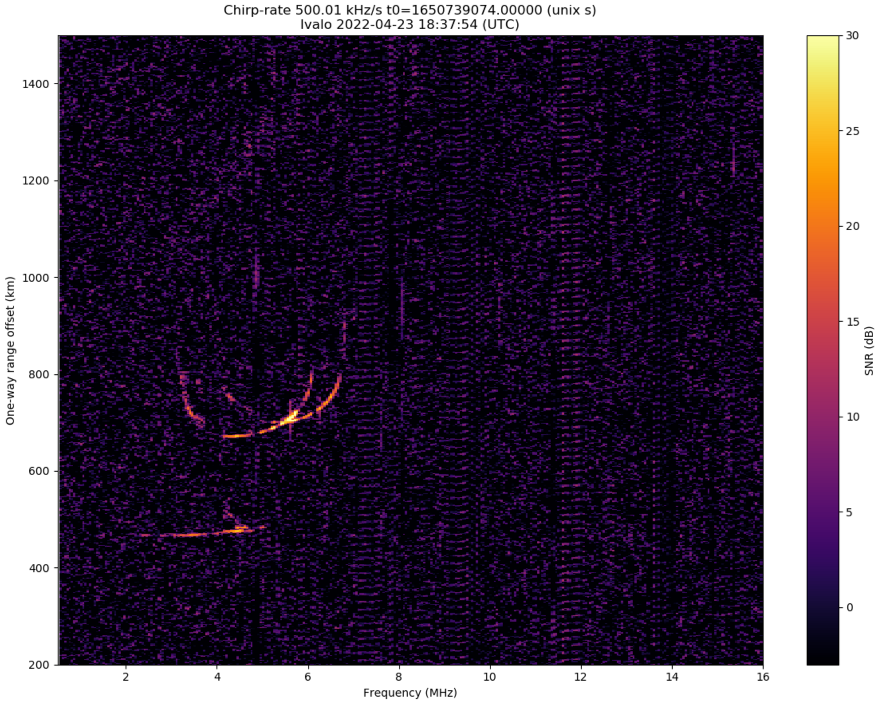

Figure 5.5: Sample ionogram collected with the OTHR4 radar receiver.

The E-region traces can be seen in figure 5.5 at a one-way range offset of around 500 km and around a frequency of 2.5 MHz. The F-region traces are also visible with distinguishable o- and x-modes starting around a one-way range offset 700 km and around a frequency of 3 MHz. The OTHR4 system appear to be fully functioning.

6

Deployment

This chapter will describe the deployment of the radar receiver systems in the field. In total, four radar receiver systems were constructed as part of this thesis project. These were deployed in four different sites, the locations geographically distributed around the transmitter in Sodankylä. The locations were chosen partially due to the geography, but also on the basis of my supervisor having contacts from Sodankylä Geophysical Observatory (SGO) at each site that could give us access to buildings for the instruments and connect us to the infrastructure on site. The installation sites are:

- Skibotn, Norway (UiT field station)
- Oulu, Finland (SGO site)
- Kuusamo, Finland (SGO site)
- Ivalo, Finland (Lassi Roininen's cabin)

The sites are also indicated on the map in figure 6.1. Also seen in figure 6.1, is the location of the transmitter in Sodankylä. The map was generated using the *cartopy* toolkit and a script written by Juha Vierinen.

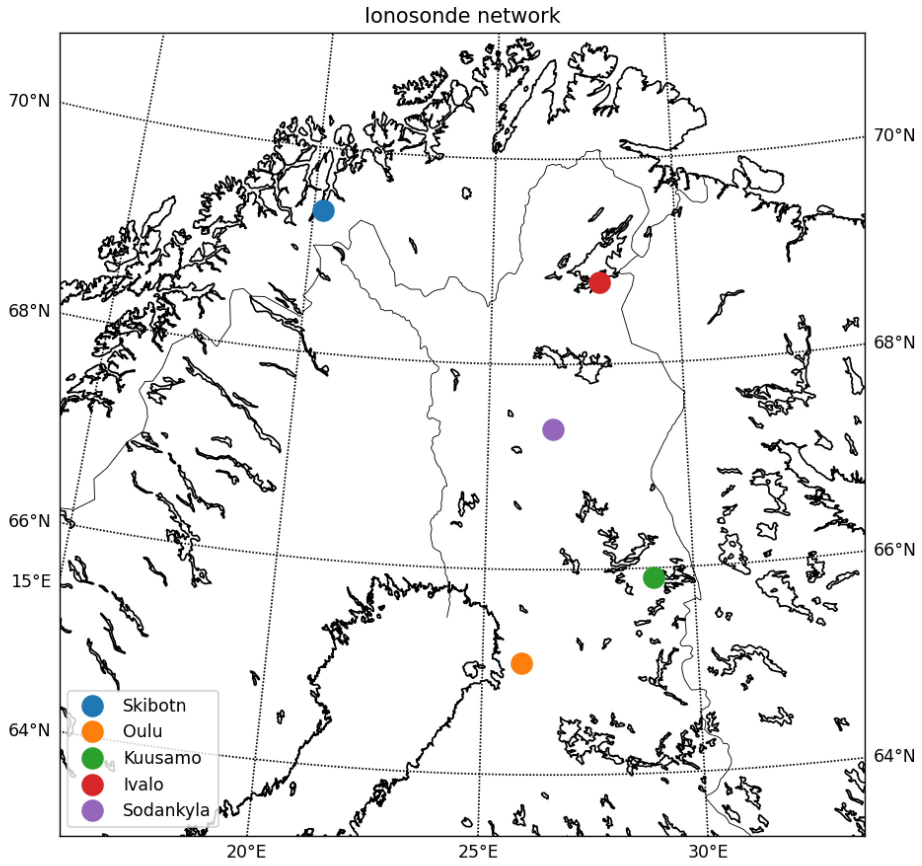

Figure 6.1: A map indicating the four locations where the radar receivers were installed, as well as the location of the transmitter in Sodankylä.

The goal is to receive single-hop radiowaves on the selected locations. The previously shown figure 2.5 displays a triangular path of a wave with one reflection in the ionosphere. The length of the travel path is the one-way range offset. In the case of a virtual path as in figure 2.5, the wave is reflected from a single point in the ionosphere, i.e. a single altitude. The one-way range offset can be used together with information on the distance between the transmitter and the sender to determine the altitude of this reflecting layer. Table 6.1 lists the distances between the transmitter in Sodankylä and each radar receiver system, as measured using the distance tool on the online map service Google Maps. The GPS coordinates for the radar receiver locations were also measured using Google Maps. With figure 2.5 in mind, we denote the distance between transmitter and receiver d_{TR} and the one-way range offset TAR. If the virtual path is triangular, we can find the virtual height of reflection h' using the Pythagorean theorem:

$$h' = \sqrt{\left(\frac{TAR}{2}\right)^2 - \left(\frac{d_{TR}}{2}\right)^2} \tag{6.1}$$

The installation in Skibotn was handled by my supervisor Juha Vierinen and myself, during a 1-day excursion to the UiT field station in Skibotn. The installations of the systems in Finland were carried out by my co-supervisor Devin Huyghebaert and myself. We went on 6-day field trip through Finland, travelling by car from site to site performing installations. Through Juha Vierinen we received aid in organizing the trip from Tomi Teppo, affiliated with SGO. Tomi made sure someone was able to meet us at each site and provide some guidelines for how the installations would be done. The following sections will describe the locations and provide photos of the installations.

Table 6.1: d_{TR}, indicating the distances between the transmitter in Sodankylä and the radar receivers at their respective locations. The GPS coordinates are given in the format (latitude, longitude). The GPS coordinates for the location of the transmitter is (67.36435 °N, 26.63044 °E).

Location	d_{TR} [km]	GPS coordinates [°]
Skibotn	338.8	69.39080 N, 20.26730 E
Oulu	255.3	65.08647 N, 25.89216 E
Kuusamo	193.1	65.91137 N, 29.04016 E
Ivalo	167.5	68.79610 N, 27.88395 E

6.1 Skibotn

Figure 6.2: The Skibotn antenna installed using pine trees as fastening points for all four guy-wires.

The radar receiver system can be seen installed in Skibotn in figure 6.2. This installation served as a test-run for the installations to come. It was the first installation, and a learning experience for the Finnish installations. The Skibotn installation shed some light on the need for a better and safer solution for powering the rack mounted case, as the solution that can be seen in figure 6.3 was not sufficient. Another thing learned here was that we should curl the coaxial cable into a loop after fastenings the N-connector but before zip-tying it to the mast in order to relieve it from mechanical stress. I also learned that the N-connector should be weatherproofed with self-vulcanizing tape, and that the mast joint should be duct-taped in order to retain some strength in the undesired event of the fiberglass tube ends start cracking.

Figure 6.3: The rack mounted case as installed on the Skibotn site (left) and a partial photo of the hut it was installed in (right) where also the active GPS antenna can be seen mounted on the end of the roof.

6.2 Oulu

The University of Oulu operates an observatory field station in the village Huttukylä nearby Oulu, where we were allowed to install one of the radar receivers. The site was readily accessible by car and hosted a series of other instruments including a rather sensitive seismometer. This means that the radar receiver must be kept at a distance to reduce interference, leading to the install location being in a corner of the plot. The trees in the plot had mostly been cut down and cleared out, so we used pegs driven into the ground to fasten the guy-wires for three points, while the last guy-wire was fastened to a small tree nearby. Keeping in mind both the radiation pattern of a small magnetic loop antenna (exhibited in figure 3.1) and the geographical location of the transmitter/receivers (as shown in figure 6.1), we oriented the directions of maximum gain in the direction pointing towards the transmitter. The cardinal directions were approximated using a cellphone compass or the Sun.

Figure 6.4: Photo of the antenna as it was installed on the Oulu site. Ground pegs were used to attach three out of four guy-wires, the last one attached to a tree.

After installing the antenna element and the GPS antenna, we routed the cables inside and started the system. We changed a setting in the BIOS in order to ensure that the computer automatically powers on in the event of a power outage. We then ran the shell script and waited for measurements while my supervisor Juha accessed the computer remotely. Before long the first ionogram could be plotted, and remote access was established. The Oulu installation was successful.

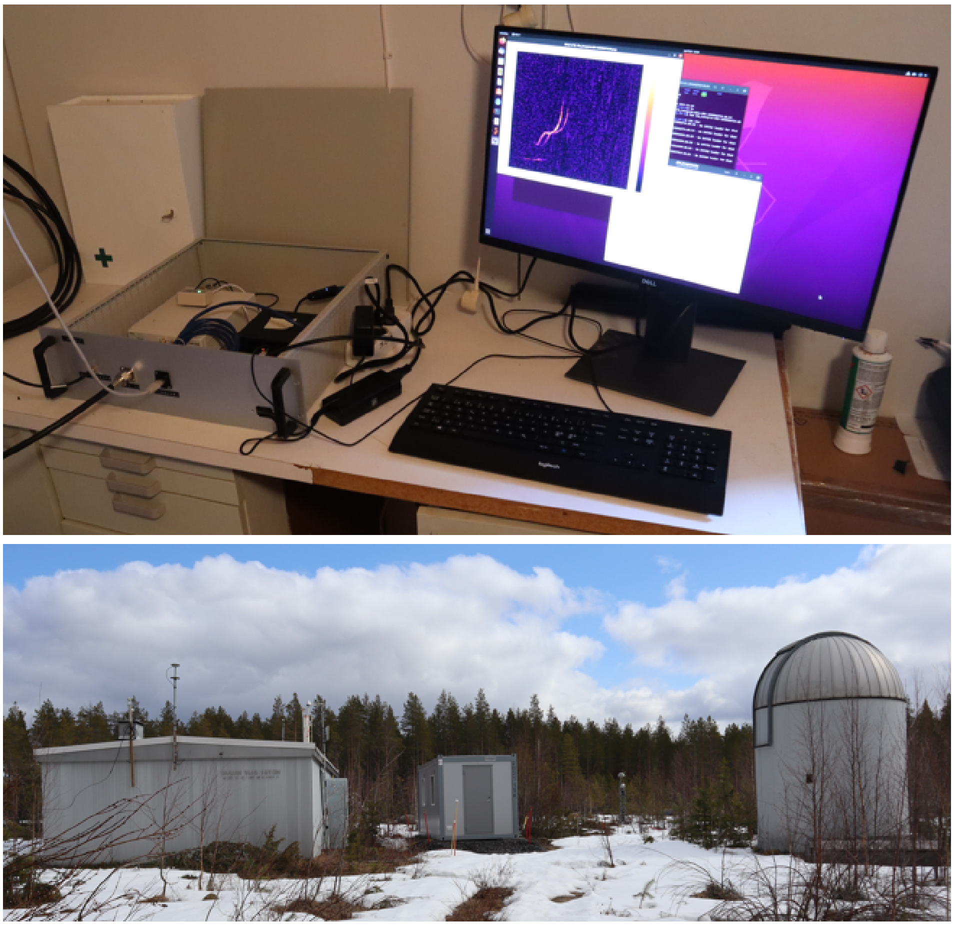

Figure 6.5: Rack mounted case for the Oulu site, photo taken during the setup of the instrument (top). Instrument shack on the Oulu observatory site the radar receiver was installed (bottom).

6.3 Kuusamo

SGO operates a field station near Kuusamo, at which we were permitted to deploy one radar receiver. The area is subject to heavy snowfall during the winter, necessitating us renting snow shoes in order to able to walk to the site. A couple of SGO technicians met us at the site to assist with the installation. They focused on routing cables inside the instrument shack and properly grounding the rack mounted case, as well as assisting with installing the GPS antenna. Meanwhile Devin and I set up the antenna element as it is shown in figure 6.6. We used trees for three of the guy-wires and ended digging a hole in the snow in order to drive a peg into the ground for fastening the fourth guy-wire.

Figure 6.6: Photo of the antenna as it was installed on the Kuusamo site. Trees were used to attach three out of four guy-wires, the last one attached to a peg driven into ground.

With the rack mounted case grounding finished and the antenna element set up, all cables were routed and the system was connected to power and ethernet. After turning on the BIOS automatic power-on setting, we established a remote connection with supervisor Juha. The shell script was executed and before long the first ionogram was plotted. The Kuusamo installation was a success.

Figure 6.7: Photos from the Kuusamo site. Rack mounted case installed in the shack (left) and the instrument shack as seen from the outside (right). The GPS antenna can be seen mounted on piece of wood in the upper left corner of the shack image.

6.4 Ivalo

The Ivalo site is on the property of a cabin owned by Lassi Roininen. He met us there for the fourth and final radar receiver installation. As this location is somewhat off-grid, we did not have access to a cabled Ethernet connection. Instead the staff of SGO equipped us with a high-grade mobile 4G router in order for us to have internet access. This was installed in proximity to the rack mounted case inside Lassi's fishing shed. The antenna element was mounted roughly 20 meters outside the shed. The ground at the site was considerably rocky, making the driving of pegs into the ground a challenge. We ended up only driving the earthen anchor into the ground and fastening all four guy-wires to nearby trees. The installed antenna can be seen in figure 6.8.

Figure 6.8: Photos of the antenna as it was installed on the Ivalo site. Trees were used to attach all four guy-wires.

After everything was installed and connected to the rack mounted case with power, the system was powered on. The 4G router was working, albeit with a rather slow upload link. We established a remote connection with Juha on the other end, and measurement could begin. After a little while the first ionogram could be plotted. The level of noise for this antenna turned out be a bit more than the other systems. We speculated that this could be interference from a nearby cell tower. At the end of the day the signal-to-noise ratio was still good enough for the purposes of the system, so we didn't pursue any remedies or further explanations.

Figure 6.9: Photos from the Ivalo site. Rack mounted case inside the fishing shed (bottom) and the fishing shed located on the cabin property (top).

7

Results and discussion

The radar receivers were successfully installed, meaning that this project has met its main goal. With the radar receivers in operation, the collection of data is a continuous event. The systems have already collected thousands of ionograms since being installed in April 2022. In this chapter, we will look at some example ionograms. We will also attempt extraction of ionospheric parameter data from an ionogram using a manual ionogram scaling program written by Juha Vierinen. The code for this program can be seen in appendix B. Lastly the chapter includes examples of frequency and range stacked ionogram data in which we will look for TIDs.

The latest captured ionogram for each of the four oblique ionosonde receivers is uploaded to an online server, address `http://soppel.org/hf/`. The code used to generate the plots can be found in this section is available at `https://github.com/jvierine/chirpsounder2`.

7.1 Ionograms from different sites

Figures 7.1, 7.2, 7.3 and 7.4 show four different ionograms collected on 25.05.2022 15:03:54 (UTC) from the four different receiver locations. The ionograms exhibit reasonable signal-to-noise ratios, and the split traces corresponding to the F region indicates that both O-mode and X-mode propagation has been measured. Inspecting the ionograms reveals that the traces are different for all four ionograms, meaning that the properties of the ionospheric region they probe are different. This is a testament to the spatial variability of the ionosphere. Investigation of the spatial variability is an important objective of this project.

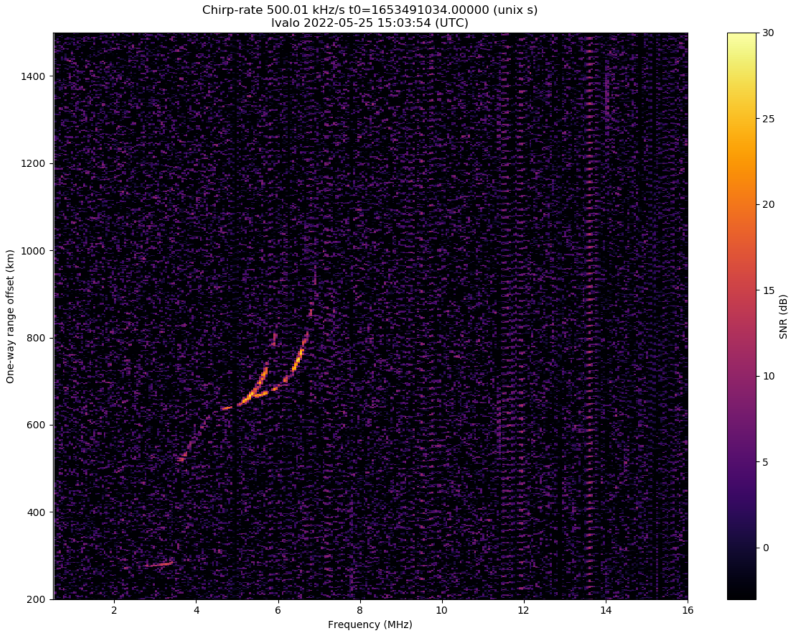

Figure 7.1: Ionogram collected on the Ivalo radar receiver on the indicated date and time.

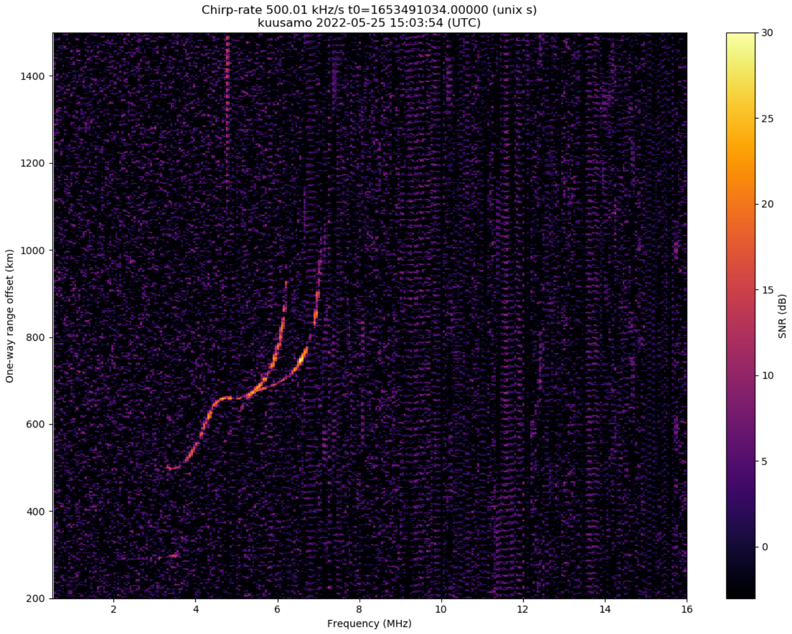

Figure 7.2: Ionogram collected on the Kuusamo radar receiver on the indicated date and time.

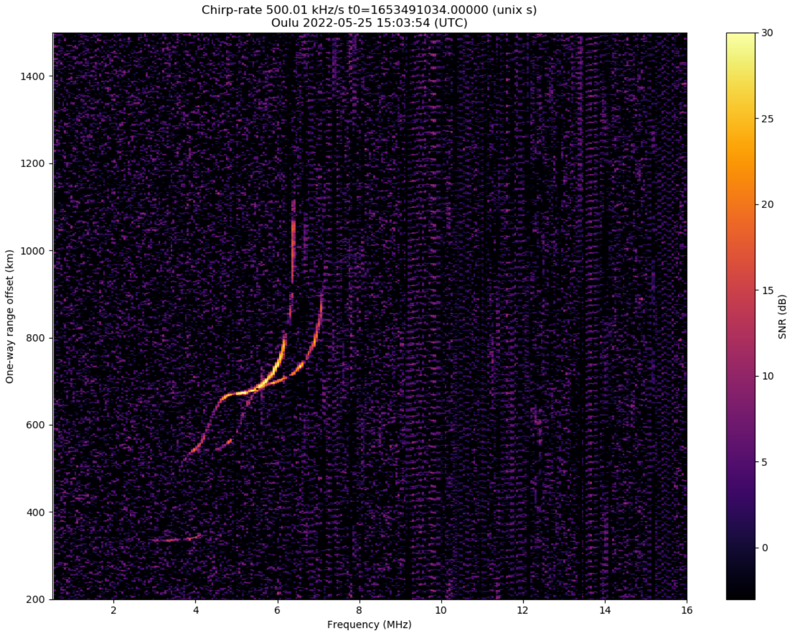

Figure 7.3: Ionogram collected on the Oulu radar receiver on the indicated date and time.

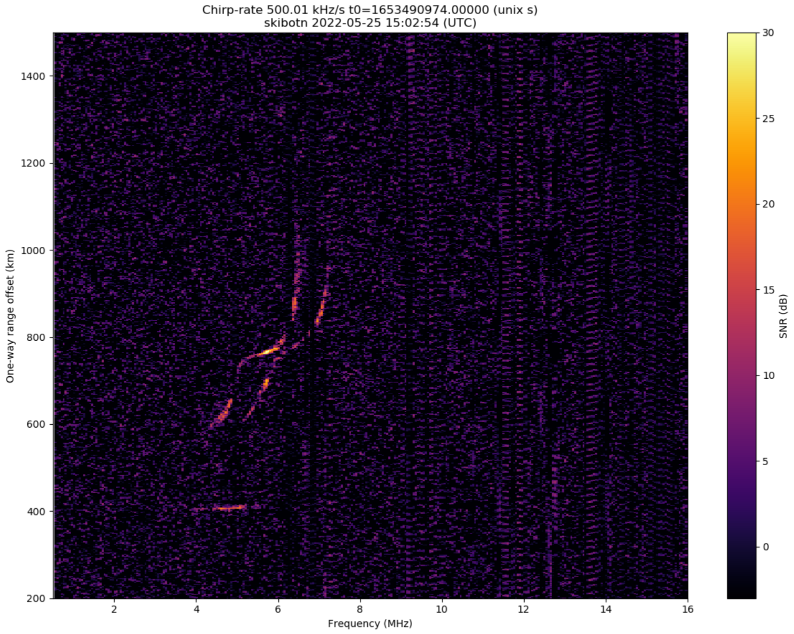

Figure 7.4: Ionogram collected on the Skibotn radar receiver on the indicated date and time.

7.2 Scaled ionogram

Using the *manual_ionogram_scaler.py* program (see appendix B), the ionospheric parameters **foF2, h'F, foE** and **h'E** were extracted from an ionogram sampled at the Kuusamo site. Visible in figure 7.5 is an ionogram that was captured by the Kuusamo radar receiver on the 02.05.2022 00:21:54.

In figure 7.6 the very same ionogram from 02.05.2022 00:21:54 has been manually scaled using the program given in appendix B, in accordance with the standard practices for scaling outlined in section 2.3.2. The red line is **foF2**, the green line is **h'F**, the blue line is **foE** and the white line is **h'E**. The critical frequencies are readily read off the figure. The virtual heights must be calculated using eq. 6.1 after obtaining the one-way range offset from the ionogram and the distance from table 6.1. The parameters for the ionogram seen in figure 7.6 are summarized in table 7.1. It appears that the radar receiver system in Kuusamo provided sufficient signal-to-noise ratio to allow for determining basic ionospheric parameters from the ionograms it produces.

Table 7.1: Ionospheric parameters and their measured/estimated values.

Parameter	Measured value
foF2 [MHz]	4.1
h'F [km]	292.5
foE [MHz]	2.2
h'E [km]	98.6

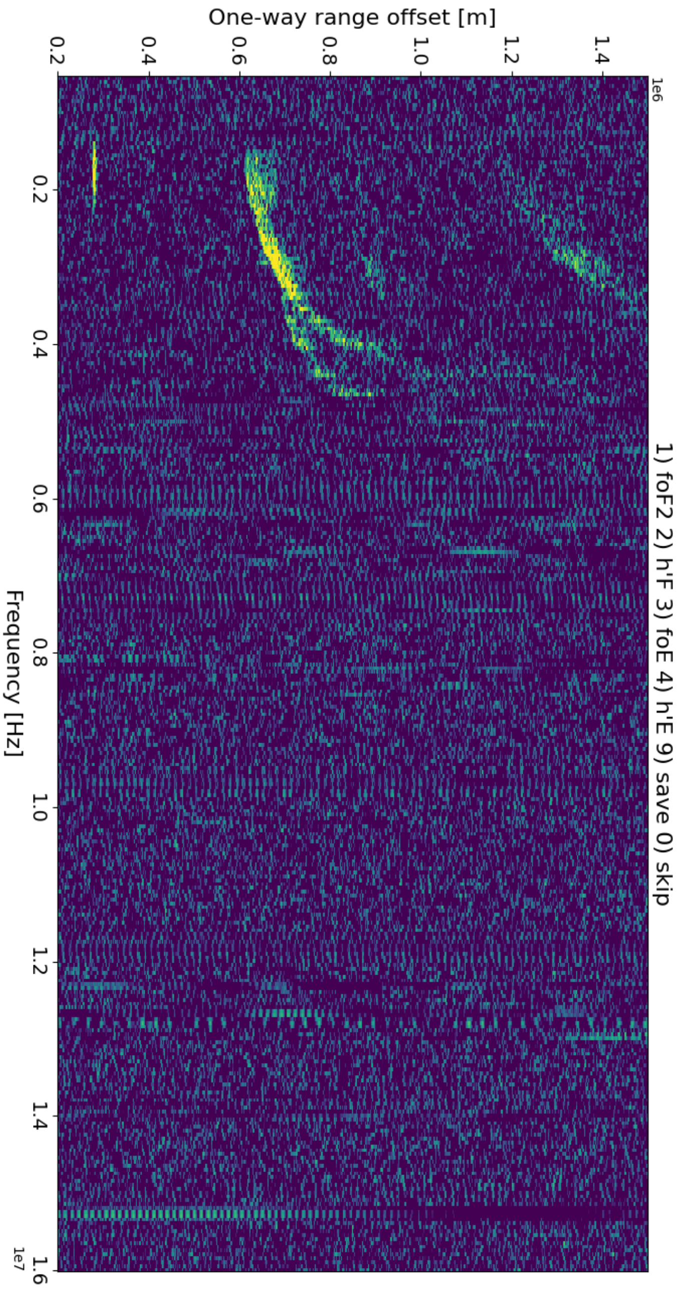

Figure 7.5: Ionogram collected on the Kuusamo radar receiver on 02.05.2022 00:21:54.

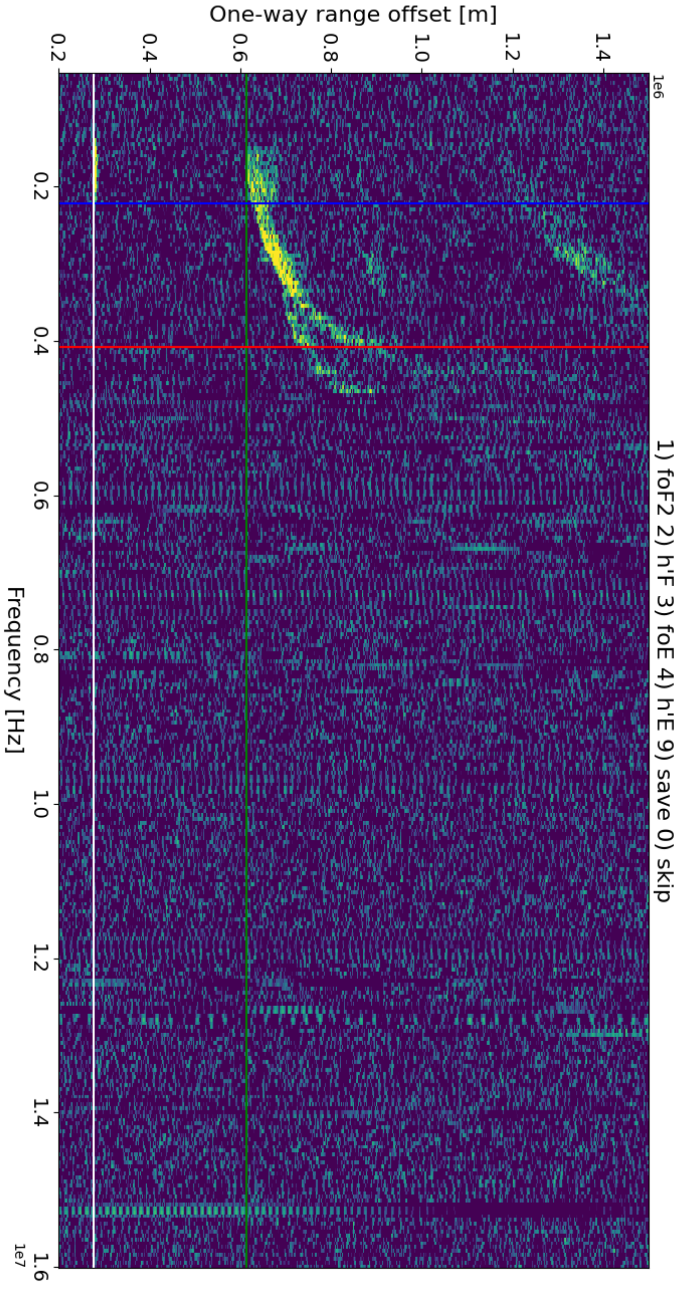

Figure 7.6: Ionogram collected on the Kuusamo radar receiver on 02.05.2022 00:21:54 and manually scaled to obtain ionospheric parameters.

7.3 Frequency stacks

In order to get a better view of how the ionospheric density structures behave temporally, we can produce a frequency stack from the ionogram data spanning a full day. This is done by making a vector of frequencies corresponding to a point in time for all ranges, and then retrieving the maximum power for each range. This is then repeated for all time points throughout a day. Such a stack can be seen in figure 7.7, collected by the Skibotn radar receiver on 21.05.2022.

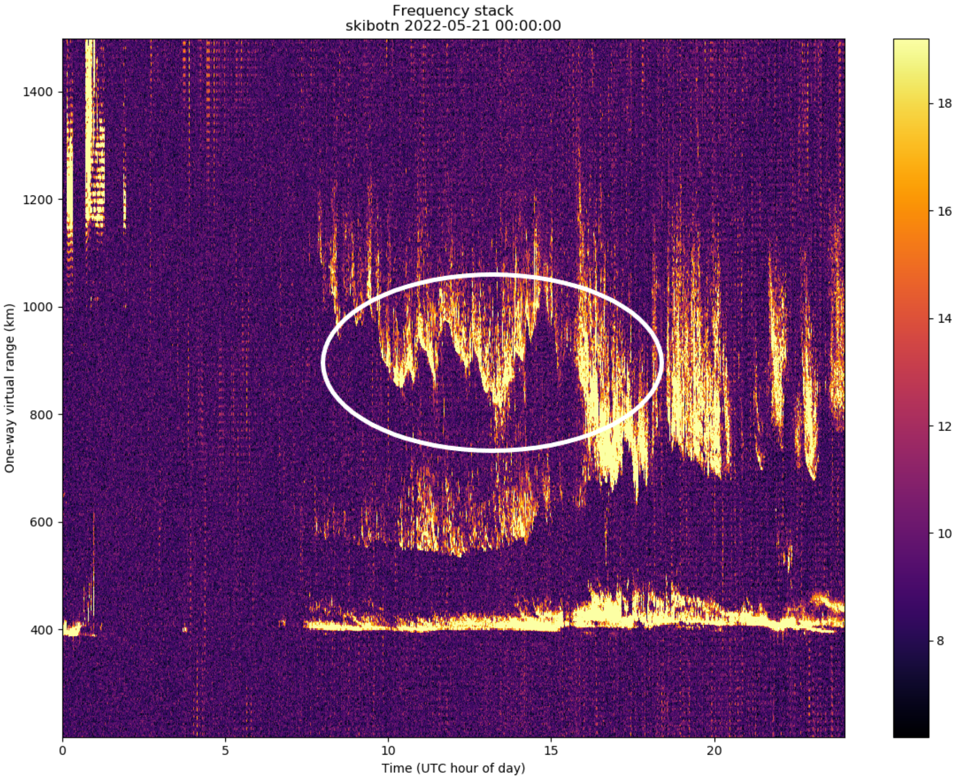

Figure 7.7: Frequency stack collected with the Skibotn system, collected on 21.05.2022.

A white ellipse is drawn in figure 7.7 to highlight what could be the signature of a travelling ionospheric disturbance (TID), as a quasi-periodic pattern in the frequency stack suggests fluctuations in the electron density.

A different approach to creating a frequency stack is treating several frequencies separately, as can be seen in figures 7.8-7.11. The plots show one-way range offset for each frequency as it varies with time, where the signal intensity is indicated by color intensity. The transparency of the pixels also vary with signal intensity. With this type of plot we may be able to see signatures of TIDs as they change the electron density structure at different altitudes. It's worth noting that these plots contain information from both O-mode and X-mode propagation.

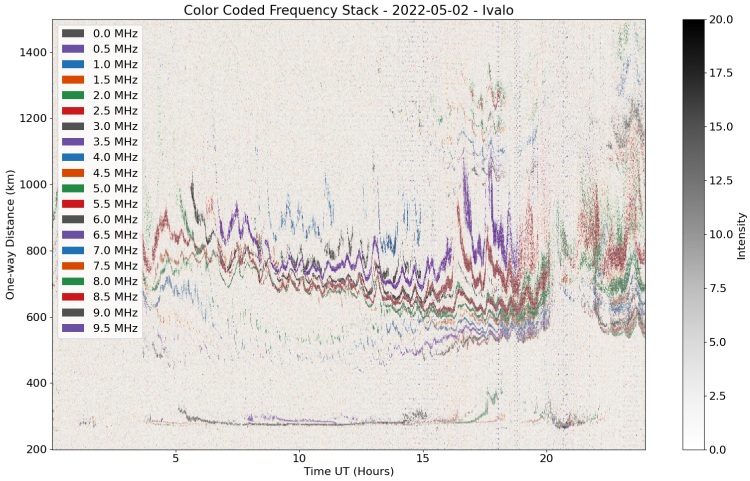

Figure 7.8: Color coded frequency stack procured from data collected on the indicated day with the Ivalo system.

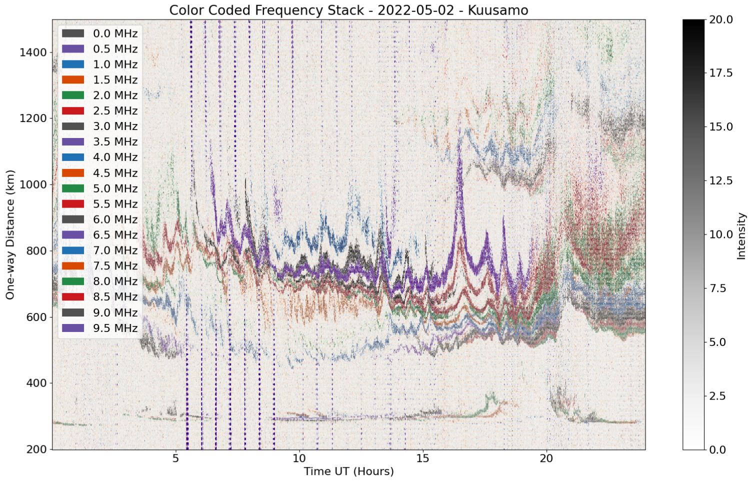

Figure 7.9: Color coded frequency stack procured from data collected on the indicated day with the Kuusamo system.

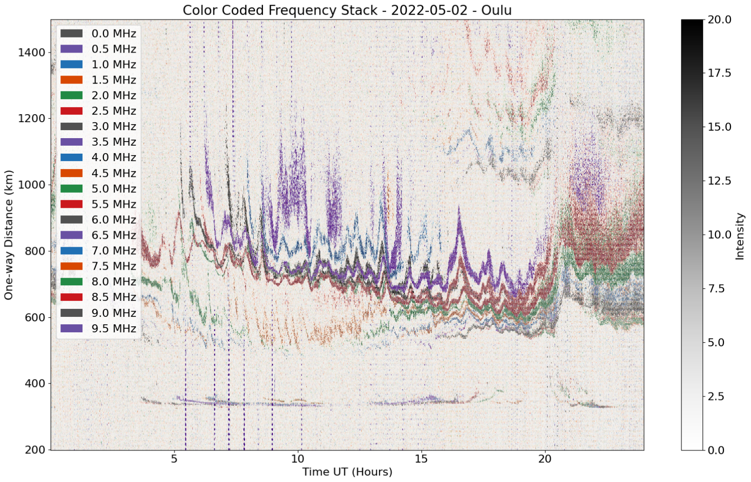

Figure 7.10: Color coded frequency stack procured from data collected on the indicated day with the Oulu system.

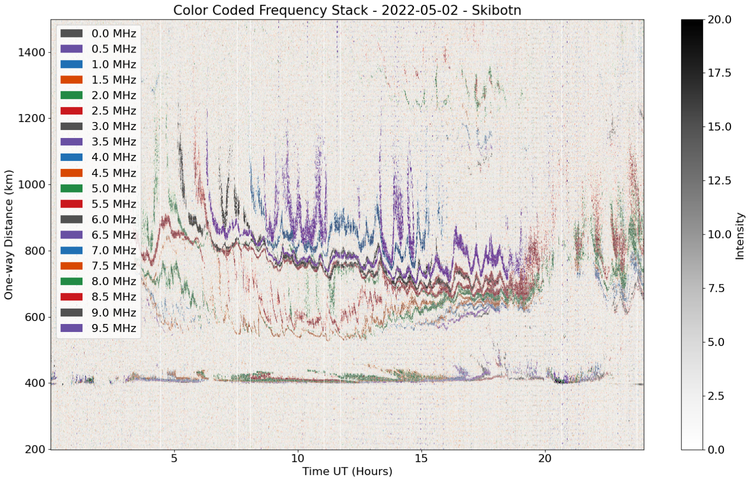

Figure 7.11: Color coded frequency stack procured from data collected on the indicated day with the Skibotn system.

One of the goals for this thesis project was to develop an instrument that could be used for ionospheric inquiry. We can look for signatures of TIDs in the color coded frequency stacks. In figures 7.9 and 7.10 we can observe a quasi-periodic fluctuation in the one-way range offset (an subsequently also a fluctuation in the corresponding virtual heights) starting at roughly 16:00 UTC. By peak-to-peak reading of the fluctuation in the plots, the period of this quasi-periodic pattern is estimated to be 60 minutes. The pattern is assumed to be the signature of a TID travelling in the ionosphere. This period is smaller but similar to the apparent period of the TID signature seen in figure 2.8 [Reinisch, 2018], which in section 2.4 was estimated to be 90 minutes.

There seems to be some quasi-periodic pattern around the same time of day in figure 7.11 as well, although the period is seemingly smaller. Distortion of the peaks make a period estimation difficult in this case without a more thorough analysis.

7.4 Range stacks

A range stack is another type of stack that gives an overview of the ionospheric conditions for a full day. The technique to procure a range stack is similar to that of a frequency stack, but now the one-way offset ranges are stacked in a vector and the maximum power has been extracted for all frequencies. This is then performed for all time points in a day for each frequency in the sweep. An example of a range stack can be seen in figure 7.12.

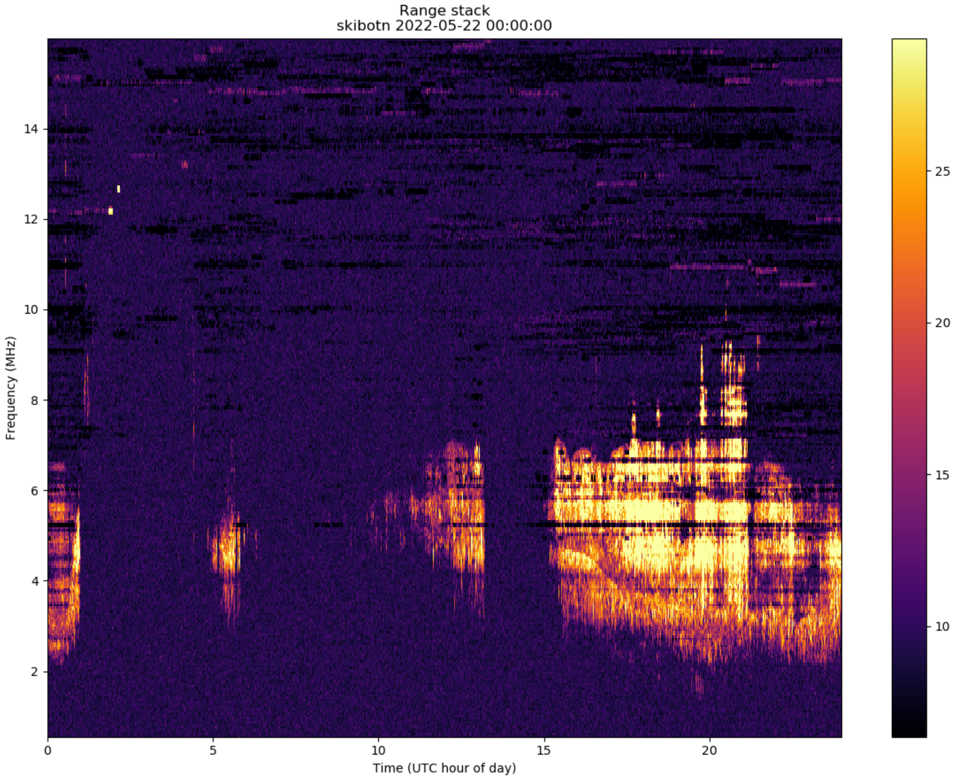

Figure 7.12: Range stack collected with the Skibotn system, collected on 22.05.2022.

In the range stack in figure 7.12, we can see stretches in time where there is almost no signal power, for example in the time frame of 01:00-05:00 UTC. This is likely due to heavy D-layer absorption, which through attenuation in the lower layers blocks the radiowaves from entering the upper layers of the ionosphere. These sudden disturbances in the ionosphere can last for a few minutes up to several hours [Moral, 2013]. A range stack also readily displays the maximum usable frequency (MUF) for the day, found at the highest frequency with an appreciable level of signal intensity (power). According to figure 7.12, the MUF for the Skibotn site at 22.05.2022 was around 9 MHz.

7.5 Range cut

Plotting a range cut, like the one seen in figure 7.13, is another method to search for signatures of TIDs. Such a plot is made by looking at a specific range, which is an F region range of 850 km in this case. The frequencies for said range varies with time, and are plotted for a 10 hour window. In figure 7.13, the frequencies for the different receiver locations are shifted by the indicated amount in order for the figure to be less cluttered and making the features of the plot easier to see (non-shifted the frequency traces would have been layered on top of each other). The intensity of the pixel color reflects the intensity of the signal. Also worth mentioning is that the plot contains the traces for both O- and X-mode propagation. In such a plot one would look for sudden changes in the frequencies that are also offset (in time) between the receiver stations. Separation in time suggest a travelling structure. Starting slightly after 13:00 UTC (indicated by the black vertical line) there is a pronounced change in the frequency. Comparing this feature of the Skibotn trace with the same feature in either the Kuusamo trace or the Oulu trace, we observe a small time delay. This time delay suggests some structure travelling from the north towards the south, affecting the frequency (through variations in the electron density) as it travels. This may be the signature of a TID. According to literature, large-scale TIDs originating in high latitudes typically travel toward the equator [Hunsucker, 1982], and this may be what is observed here.

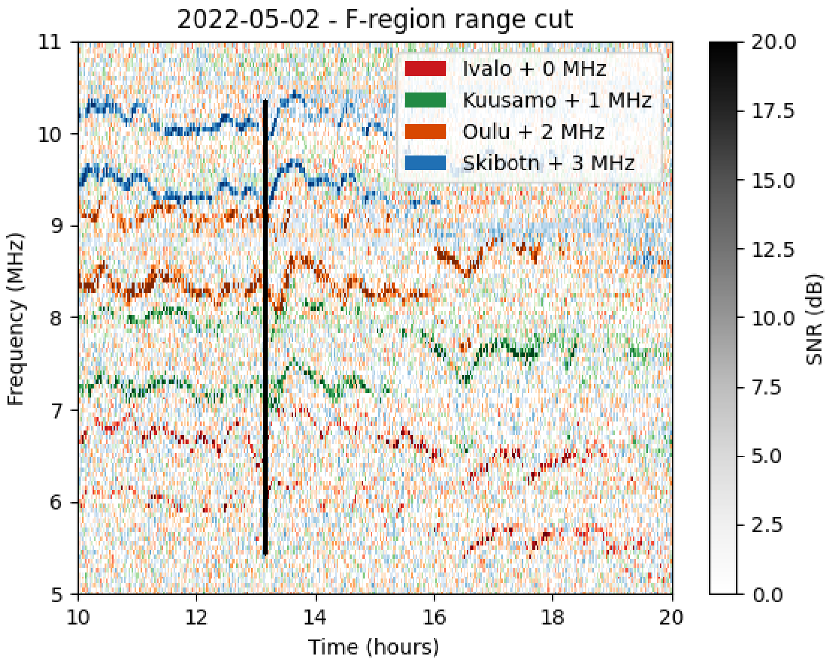

Figure 7.13: Range slice procured from measurements from all 4 receiver locations on 02.05.2022.

8

Conclusions

1. An oblique ionosonde receiver was designed and implemented using commercially available and/or easily manufactured components, then tested to be functional in a laboratory setting.

2. Four systems were built according to the tested design and deployed in four locations geographically distributed around a transmitter in Sodankylä. All four systems are functional and are continually making oblique measurements of the ionosphere with 1 minute temporal resolution.

3. The collected data has been demonstrated to be of sufficient quality for extraction of basic ionospheric parameters such as **foF2**, **h'F**, **foE** and **h'E**. Efforts were made to observe the signatures of travelling ionospheric disturbances in the data.

Future work

The oblique ionosonde receivers currently in operation enable the extraction of basic ionospheric parameters. In this work the parameter extraction was performed using a manual ionogram scaling program. Further work could involve implementation of automatic parameter extraction using deep-learning reinforced scaling techniques. With efficient automatic scaling, further work could also involve the creation of a monitoring or forecasting service that reports the ionospheric conditions in almost real-time.

The data produced by the current network of ionosonde receivers can be used to investigate travelling ionospheric disturbances, enabling researchers with access to the data to further deepen our collective understanding of atmospheric gravity waves and their effect on ionospheric dynamics. Including TID monitoring in a forecasting service may also be beneficial, due to the effects of TIDs on radiowave propagation conditions in the ionosphere [Verhulst, 2017].

With a functional oblique ionosonde receiver design that is simple and relatively inexpensive to manufacture, the threshold is lowered for future expansion of the network in terms of the number and density of receivers. Incorporation of more receivers in the network improves coverage and spatial resolution. An expansion will also improve the diagnostic capabilities of the network in the event of a monitoring and/or forecasting service being developed. Further work may also include configuring the network to cooperate with multiple transmitters. The wide-band reception of this ionosonde receiver also permits detection of other HF signals, meaning that this system also has the potential to serve as a receiver in other radar experiments, such as DARN/SUPERDARN [Greenwald, 1995].

A

Software setup and making measurements

A.1 Dependencies installation

Running the commands given in this section will install all the necessary packages and libraries that the software depends on.

dependencies.txt

This file can be found here: `https://github.com/jvierine/chirpsounder2/blob/980e34c931e5d0459d97acb6c0f81b9312edfc77/dependencies.txt`

```
sudo apt install git
sudo apt-get install libhdf5-dev
sudo apt-get install cmake
sudo apt-get install python-mako
sudo apt-get install python-numpy
sudo apt-get install python-pkgconfig
sudo apt-get install python3
sudo apt-get install python-setuptools
sudo apt-get install python-h5py
```

```
sudo apt-get install python-packaging
sudo apt-get install python-tz
sudo apt-get install python-dateutil
sudo apt-get install gnuradio
sudo apt-get install python-matplotlib
sudo apt-get install python-scipy
sudo apt-get install python3-uhd
sudo apt install python3-pip

sudo apt install python3-h5py
sudo apt install python3-mpi4py
sudo apt install python3-pyfftw
sudo apt install python3-watchdog

# install ntp client to sync PC clock to network
sudo apt-get install chrony

pip3 install uhd
sudo apt-get install libgnuradio-uhd

git clone http://github.com/MITHaystack/digital_rf
cd digital_rf/
mkdir build
cd build
cmake ..
make
sudo make install

cd ~/
sudo apt-get install libboost-all-dev libusb-1.0-0-dev doxygen
↪  python3-docutils python3-mako python3-numpy
↪  python3-requests python3-ruamel.yaml python3-setuptools
↪  cmake build-essential
git clone https://github.com/EttusResearch/uhd.git
cd uhd/host/
mkdir build
cd build
cmake -DENABLE_PYTHON=ON ..
make
sudo make install

# refresh shared library index
sudo ldconfig
```

```
#
git clone http://github.com/jvierine/chirpsounder2
cd chirpsounder2/
make

#Use pip3 to install missing packages (e.g. pyfftw, scipy
↪  etc.). shouldn't be needed
#Thor can be tested using the suggested line "thor.py -m
↪  192.168.10.2 -d "A:A" -c cha -f 12.5e6 -r 25e6
↪  /dev/shm/hf25"

# create data output directory. ionograms will go here
sudo mkdir -p /data0
sudo chown -R $USER:$USER /data0
```

A.2 Making a measurement

Making a measurement is done by executing the *sgo.sh* shell script below, which in turn starts all the necessary processes to make measurements. The *sgo.sh* shell script uses configurations from the *sgo.ini* file, which is given below as well.

sgo.sh

This file can be found here: `https://github.com/jvierine/chirpsounder2/blob/980e34c931e5d0459d97acb6c0f81b9312edfc77/examples/sgo/sgo.sh`

```
#!/usr/bin/bash
#
# start a ringbuffer
#
INSTALL_PATH=/home/hfrx2/src/chirpsounder2
cd $INSTALL_PATH
# stop all processes
./stop_ringbuffer.sh
CONFFILE=/home/hfrx2/src/chirpsounder2/examples/sgo/sgo.ini
DDIR=/dev/shm/hf25
mkdir -p logs
```

```
# delete old data from ram disk
rm -Rf $DDIR
mkdir -p $DDIR

# sync to ntp time not needed, if you run ntpd
#echo "NTPDATE"
#sudo ntpdate ntp.uit.no

# setup ringbuffer
echo "Ringbuffer"
drf ringbuffer -z 30000MB $DDIR -p 2 >logs/ringbuffer.log 2>&1
↪  &


# Calculate ionograms using known timings
# use two parallel threads. one for SGO and one for HAARP
echo "Ionogram calc"
python3 calc_ionograms.py $CONFFILE >logs/calc_ionograms.log
↪  2>&1 &
sleep 10

# plot ionograms
echo "Plot ionograms"
python3 plot_ionograms.py $CONFFILE >logs/plot_ionograms.log
↪  2>&1 &

while true;
do
    echo "Starting THOR"
    # start digital rf acquisition with custom c++ program
↪   that uses the uhd driver directly, skipping gnuradio
    ./rx_uhd >logs/thor.log 2>&1
    sleep 10
done
```

sgo.ini

This file can be found here: `https://github.com/jvierine/chirpsounder2/blob/980e34c931e5d0459d97acb6c0f81b9312edfc77/examples/sgo/sgo.ini`

```
#
# Ringbuffer mode data acquisition for the travelling
↪  ionospheric
# disturbance phase velocity and scale size campagin.
#
# Listen to the Sodankyla 500 kHz/s ionosonde transmitter,
↪  which has
# known timing, so no search is needed.
#
[config]

# specify that processing occurs on a live ringbuffer
# that continuously gets added more measurements by
# the recorder (and old files are removed to keep buffer a
↪  constant size)
# this requires the processing to sometimes wait for more data

station_name="skibotn"

realtime=true

# recording settings and data directory
channel="cha"
sample_rate=25000000.0
center_freq=12.5e6
# use ram dis
data_dir="/dev/shm/hf25"

output_dir="/data0"

save_raw_voltage=false

# ionogram calc
range_resolution=2e3
frequency_resolution=50e3
max_range_extent=1000e3

# this should be only large enough that the chirp calculation
# is performed in real-time
n_downconversion_threads=2
decimation=1250

# plot
```

```
min_range=200e3
max_range=1500e3
manual_range_extent=true
min_freq=0.5e6
max_freq=16e6
manual_freq_extent=true

# display the detected ionograms
plot_timings=false
debug_timings=false

copy_to_server=true
copy_destination="j@eetu.no:/var/www/soppel.org/hf"

#
# Listen to two sounders in parallel
#
# 1) Sodankylä 500 kHz/s sounder at 0.0016 s mean propagation
↪   delay
#
#        [{"chirp-rate":500.0084e3,"rep":60.0,"chirpt":54.0016,"id":1}]
sounder_timings=[

        [{"chirp-rate":500.0084e3,"rep":60.0,"chirpt":54.0,"id":1}]
       ]
```

/B

Manual ionogram scaling program

The manual ionogram scaling program given below is used to manually extract the a handful of ionospheric parameters from an ionogram. The critical frequencies and virtual heights are selected using the mouse to aim and the number keys on the keyboard to capture the (x,y) coordinate in the plot. A horizontal or vertical line is then drawn in the plot to indicate the value of the parameter. Considering that the y-axis is the one-way range offset then

```
import imageio
import matplotlib.pyplot as plt
import glob
import sys
import h5py
import os
import numpy as n
from pathlib import Path

# Label ionogram manually using a mouse and a keyboard

# if true, plot all scaled ionograms.
# otherwise scale only unscaled ionograms,
# skipping already labeled ionograms
```

```
review=True

fl=glob.glob(r("C:\Users\jensf\Desktop\Results\
2022.05.02.tar\ski\2022-05-02\*.h5"))

fl.sort()

def normalize(S):
    for fi in range(S.shape[0]):
        noise_floor=n.median(S[fi,:])
        std_floor=n.median(n.abs(S[fi,:]-noise_floor))
        S[fi,:]=(S[fi,:]-noise_floor)/std_floor
    S[S<0]=1e-3
    return(S)

for f in fl:
    hin=h5py.File(f,"a")
    print(hin.keys())

    S=normalize(hin["S"][()])
    freqs=hin["freqs"][()]
    ranges=hin["ranges"][()]

    fig, ax = plt.subplots(figsize=(18,12))

    fof2=0.0
    hf=0.0
    fe=0.0
    he=0.0

    if "hf" in hin.keys():
        hf=hin["hf"][()]
        ax.axhline(hf,color="green")
        fig.canvas.draw()

    if "fof2" in hin.keys():
        fof2=hin["fof2"][()]
        ax.axvline(fof2,color="red")
        fig.canvas.draw()


    if "fe" in hin.keys():
        fe=hin["fe"][()]
        ax.axvline(fe,color="blue")
```

```
    fig.canvas.draw()


if "he" in hin.keys():
    he=hin["he"][()]
    ax.axhline(he,color="white")
    fig.canvas.draw()

dB=10.0*n.log10(n.transpose(S))
dB[dB<-3]=-3
dB[dB>20]=20


def press(event):
    global fof2, hf, he, fe
    x, y = event.xdata, event.ydata
    print("press %f %f"%(x,y))
    sys.stdout.flush()
    if event.key == '1':
        fof2=x
        ax.axvline(fof2,color="red")
        fig.canvas.draw()

    if event.key == '2':
        hf=y
        ax.axhline(hf,color="green")
        fig.canvas.draw()

    if event.key == '3':
        fe=x
        ax.axvline(fe,color="blue")
        fig.canvas.draw()

    if event.key == '4':
        he=y
        ax.axhline(he,color="white")
        fig.canvas.draw()

    if event.key == '5':
        he=0.0
        fe=0.0
        hf=0.0
        fof2=0.0
        fig.canvas.draw()
```

```
        if event.key == '9':
            print("saving %s %f %f %f %f"%(f,fof2,hf,fe,he))
            hin["fof2"]=fof2
            hin["hf"]=hf
            hin["fe"]=fe
            hin["he"]=he
            hin.close()
            plt.close()

        if event.key == '0':
            print("skiping %s"%(f))
            hin.close()
            plt.close()

    fig.canvas.mpl_connect('key_press_event', press)
    ax.pcolormesh(freqs,ranges,dB)
    plt.title("1) foF2 2) h'F 3) foE 4) h'E 9) save 0) skip", fontsize=16)
    plt.xlabel("Frequency [Hz]", fontsize=16)
    plt.ylabel("One-way range offset [m]", fontsize=16)
    plt.tick_params(axis='both', which='major', labelsize=14)
    plt.show()

    try:
        hin.close()
    except:
        print("couldn't close h5 file. maybe already closed")
```

/C

Parts list and costs

Parts list

Component type	Model	Vendor	Approx. price (NOK)
SDR	USRP N200	Ettus Research	21000
RF daughterboard	LFRX 0-30 MHz Rx	Ettus Research	1100
GPSDO	GPSDO Kit for N200/N210	Ettus Research	10400
GPS antenna	NT-1575-WHT TNC	RS Components AS	900
GPS antenna cable	Siretta, Male TNC to Male SMA, RF LLC200A 50 Ω, 10 m	RS Components AS	500
Computer	ASUS PN51	Dustin	4500
RAM	Kingston, 64GB 2,666MHz DDR4 SDRAM	Dustin	2900
SSD	WD Black SN750 1000GB M.2 2280 PCI-E	Dustin	1200
Pre-amplifier w/bias-tee	MLA-30+	Hisonauto (eBay)	300
Low-pass filter	SLP-30+	MiniCircuits	400
Rack mounted case	RS HD3U466	RS Components AS	800

Coax cable	RG-213U, 50 Ω, male N-connectors	Simarud Electronics AS	3400
Fiberglass mast	2x2.38m, Ø66,ø59	Eidolon AS	1800
N-connector for pre-amp	Radiall R161325000, 50 Ω	Farnell Norge	100
Earthen anchor	Stainless steel, 75x75 mm base and 0.75m peg	Biltema	50
Guy-wiring	Custom, M8 ring bolts and synthetic rope	Biltema	350
SMA-SMA panel adapter	161-5400	RS Online	100
SMA-N panel adapter	716-4805	RS Online	600
Ethernet panel adapter	916-0255	RS Online	100
Miscellanous	Nuts, bolts, cables, zip-ties etc.	RS Online	500
Loop antenna	Custom from Ø20 mm pipe	Faculty workshop	N/A*
Mast mount	Custom plastic plate w/ Ø5mm U-bolts	Faculty workshop	N/A*
Mast joint	Machined aluminium fitting	Faculty workshop	N/A*

* these items were manufactured by the faculty workshop who did not charge us internally, but they provided a maximum estimate of 2500 NOK for all the parts for one receiver

Bibliography

[Balanis, 2016] Balanis (2016). *Antenna Theory - Analysis and Design*. John Wiley and Sons Inc, Hoboken New Jersey, 4 edition.

[Belehaki, 2020] Belehaki (2020). An overview of methodologies for real-time detection, characterisation and tracking of traveling ionospheric disturbances developed in the techtide project. 10. Journal of Space Weather and Space Climate.

[Blaunstein, 2008] Blaunstein (2008). *IONOSPHERE AND APPLIED ASPECTS OF RADIO COMMUNICATION AND RADAR*. CRC Press.

[Breit, 1926] Breit (1926). A test of the existence of the conducting layer. 28. Physical Review.

[Brekke, 2013] Brekke (2013). *Physics of the Upper Polar Atmosphere*. Springer-Verlag, Berlin Heidelberg.

[Chapman, 1931] Chapman (1931). The absorption and dissociative or ionizing effect of monochromatic radiation in an atmosphere on a rotating earth. 43(1). Proceedings of the Physical Society.

[Chen, 1983] Chen (1983). *Introduction to plasma physics and controlled fusion*. Springer Science+Business Media, New York, 2 edition.

[Davies, 1965] Davies, K. (1965). *Ionospheric radio propagation*, volume 80. US Department of Commerce, National Bureau of Standards.

[EttusResearch, 2022a] EttusResearch (2022a). Installing the ettus research™ gpsdo kit for usrp™ n200 series & e100 series. Retrieved from `https://www.ettus.com/wp-content/uploads/2019/01/gpsdo-kit_4.pdf`.

[EttusResearch, 2022b] EttusResearch (2022b). Usrp n2007n210 networked series. Retrieved from `https://www.ettus.com/wp-content/uploads/2019/01/07495_Ettus_N200-210_DS_Flyer_HR.pdf`.

[Greenwald, 1995] Greenwald (1995). Darn/superdarn. 71. Space Sci Rev.

[Heitmann, 2020] Heitmann (2020). *Characterising Spatial and Temporal Ionospheric Variability with a Network of Oblique Angle-of-arrival and Doppler Ionosondes*. University of Adelaide, School of Physical Sciences.

[Hocke, 1996] Hocke (1996). A review of atmospheric gravity waves and travelling ionospheric disturbances. 14. Annales Geophysicae.

[Hunsucker, 1982] Hunsucker (1982). Atmospheric gravity waves generated in the high-latitude ionosphere: A review. 20. Reviews of Geophysics and Space Physics.

[Ivanov, 2003] Ivanov (2003). Chirp ionosonde and its application in the ionospheric research. 46(11). Radiophysics and Quantum Electronics.

[Jonah, 2018] Jonah (2018). Tid observations and source analysis during the 2017 memorial day weekend geomagnetic storm over north america. 123. Journal of Geophysical Research: Space Physics.

[Kelley, 2009] Kelley (2009). *The Earth's Ionosphere - Plasma Physics and Electrodynamics*. Academic Press, 2 edition.

[Kirkwood, 2000] Kirkwood (2000). High-latitude sporadic-e and other thin layers–the role of magnetospheric electric fields. 91. Space Science Reviews.

[Lichvar, 2021] Lichvar (2021). chrony - introduction. `https://chrony.tuxfamily.org/`.

[Mobilemark, 2022] Mobilemark (2022). Gps-only, heavy duty timing 1575 mhz. Retrieved from `https://docs.rs-online.com/3d0b/0900766b815c8c31.pdf`.

[Moral, 2013] Moral (2013). Sudden ionospheric disturbances and their detection over istanbul. IEE - 6th International Conference on Recent Advances in Space Technologies (RAST).

[Perkins, 1973] Perkins (1973). Spread f and ionospheric currents. 78. Journal of Geophysical Research.

[Piggott, 1978] Piggott (1978). *U.R.S.I. handbook of ionogram interpretation and reduction*. International Union of Radio Science - United States, Environmental Data Service.

[Reinisch, 1978] Reinisch (1978). The universal digital ionosonde. 13. Radio Science.

[Reinisch, 2018] Reinisch (2018). Pilot ionosonde network for identification of traveling ionospheric disturbances. 53. Radio Science.

[SGO, 2019] SGO (2019). Ionosonde instrument description - alpha-wolf. Retrieved from `https://www.sgo.fi/Data/Ionosonde/ionDescr.php` on 22.05.2022.

[Shankar, 2016] Shankar (2016). *Fundamentals of Physics II - Electromagnetism, Optics, and Quantum Mechanics*. Yale University Press.

[Verhulst, 2017] Verhulst (2017). Vertical and oblique hf sounding with a network of synchronised ionosondes. 60. Advances in Space Research.

[Vierinen, 2022] Vierinen (2022). Chirpsounder 2. Retrieved from `https://github.com/jvierine/chirpsounder2`.

[Wakai, 1987] Wakai (1987). *Manual of Ionogram Scaling*. Radio Research Laboratory - Ministry of Posts and Telecommunications Japan, 3 edition.

[Xiao, 2020] Xiao (2020). Deep-learning for ionogram automatic scaling. 66. Advances in Space Research.

[Zabotin, 2005] Zabotin (2005). Dynasonde 21 principles of data processing, transmission, storage and web service. Proceedings of the Ionospheric Effects Symposium.